Title: Antidepressants reactivate developmental plasticity through remodeling of extracellular matrix

Authors: Phi T. Nguyen[1,2]*, Emily Sun[1,2], Yuecheng Shi[1,2], Shogo Tamura[1], Yang Xiao[3,4], Clay Lacefield[1,2], Gergely F. Turi[1,2], René Hen[1,2]*

Affiliations:

[1] Departments of Psychiatry and Neuroscience, Columbia University Irving Medical Center; New York, NY 10032, USA

[2] Division of Systems Neuroscience, New York State Psychiatric Institute; New York, NY 10032, USA

[3] Department of Biomedical Engineering, Columbia University; New York, NY 10027, USA

[4] Department of Systems Biology, Columbia University Irving Medical Center; New York, NY 10032, USA

*Corresponding author. Email: pn2381@cumc.columbia.edu (P.T.N.); rh95@cumc.columbia.edu (R.H.)

Abstract: Selective serotonin reuptake inhibitors (SSRIs) are widely used to treat mood and anxiety disorders, yet their molecular mechanisms of action remain poorly understood. Here, we show that chronic treatment with the SSRI fluoxetine reinstates a developmental plasticity program in the dentate gyrus (DG) by remodeling the extracellular matrix (ECM). Fluoxetine elicited a robust transcriptomic response in the DG, where mature granule cells adopted a juvenile-like profile. This shift was characterized by upregulation of the transcription factor SOX11 and the neurotrophic factor BDNF, as well as decreased ECM and enhanced structural remodeling of granule cell axon terminals. Direct enzymatic degradation of ECM in the DG reactivated SOX11 in mature granule cells. At the behavioral level, fluoxetine mitigated stress-induced fear generalization, an endophenotype of mood and anxiety disorders. This effect was phenocopied by ECM degradation, suggesting that ECM remodeling and granule cell rejuvenation are key mechanisms underlying the effects of fluoxetine, and possibly other antidepressants, on fear generalization.

Main Text: Mood and anxiety disorders, including major depressive disorder (MDD), are among the most prevalent mental illnesses and a leading cause of disability worldwide (*1*). Although selective serotonin reuptake inhibitors (SSRIs) like Fluoxetine (Flx) have been widely used as a first-line treatment for decades, they achieve remission in less than half of patients (*2*). Furthermore, SSRIs take weeks to months to achieve their full therapeutic effects. This limited efficacy underscores the critical need to better understand the cellular and molecular substrates driving an antidepressant effect.

Imaging and post-mortem studies suggest that the hippocampus plays a crucial role in the pathophysiology of mood disorders (*3,4*). In animal models, the dentate gyrus (DG) region of the hippocampus has been identified as a key area mediating the antidepressant-like effects of Flx. The DG consists of a heterogeneous population of neurons, including mature granule cells and newly generated immature granule cells arising from adult hippocampal neurogenesis. While

both cell types are essential for the antidepressant-like effects of chronic Flx treatment (*5–7*), the underlying cellular and molecular mechanisms remain poorly understood.

The extracellular matrix (ECM) is a complex glycoprotein network that stabilizes synapses and limits plasticity in the mature brain. For example, formation of the ECM plays a key role in closing neurodevelopmental critical periods, where experience-dependent refinement of neural circuits is at its peak (*8*). Emerging evidence suggests that the ECM is not a static structure, but rather a dynamic component of neural plasticity in the adult brain that can be influenced by both stress and antidepressant treatment (*9–12*). Both enzymatic ECM removal and Flx treatment reactivate features of critical period plasticity (*13–18*), but the underlying processes and whether they are related to antidepressant efficacy is unclear. In this study, we investigated the neural and non-neural substrates underlying Flx's effects in the hippocampus using animal behavior, single nuclei transcriptomic profiling, and detailed structural analyses of the ECM.

Results

Fluoxetine mitigates stress-induced fear generalization in a mouse model

To investigate the cellular mechanisms by which SSRIs modify stress-related behaviors, we used an established mouse model of chronic stress and Fluoxetine (Flx) treatment (**Fig. 1A**). Elevated glucocorticoid levels are a hallmark of mood and anxiety disorders (*19*). Accordingly, chronic corticosterone (Cort) treatment in rodents induces anxiety and depression-like behavioral impairments (*7*). Mice were exposed to Cort for 3 weeks before a subgroup received either short-term (5 days) or long-term (3 weeks) Flx treatment. In the elevated plus maze (EPM), Cort-treated mice showed reduced exploration of the anxiogenic open arm, which was reversed by 3 weeks of Flx (**Fig. 1B**, and **Fig. S1A**). However, no difference was observed after 5 days of Flx, mirroring the delayed onset of therapeutic effects in patients. Similarly, in the novelty-suppressed feeding (NSF) test, an anxiety-related conflict test, Cort-treated mice showed an increased latency to feed in the anxiogenic arena. This effect was reversed by 3 weeks of Flx treatment, but not by 5 days of treatment (**Fig. 1C**, and **Fig. S1B**).

Mood and anxiety disorders are often characterized by impaired emotional memory function, including increased fear generalization and a bias towards remembering negative information (*20,21*). In addition to measuring anxiety-related behaviors, we used a contextual fear generalization task to investigate stress-related deficits in emotional memory function. Mice were fear conditioned to an arena with a 2s footshock (context A) over three days and then exposed to the conditioned context followed by an unconditioned arena with similar contextual features (context B; **Fig. 1D**). We then measured their ability to discriminate between the two contexts at 1 and 14 days post-training by measuring freezing levels (**Fig. 1E-F**, and **Fig. S1C**). Mice in the Vehicle group showed normal memory recall and the ability to differentiate between contexts A and B, although this ability declined by day 14, reflecting memory generalization over time. Cort-treated mice could discriminate on day 1, but this ability was eliminated by day 14. This stress-induced increase in fear memory generalization was reversed after 3 weeks of Flx treatment. These effects were not due to contextual habitation and were present in both sexes (**Fig. S1D-F**). Interestingly, Cort treatment increased global freezing levels, which was also reversed by Flx treatment. In summary, our data establish a mouse model for investigating the cellular substrates through which Flx modifies stress-induced emotional memory deficits.

Time-dependent transcriptomic reprogramming in dentate granule cells after fluoxetine treatment

The hippocampus is a critical structure for emotional memory precision and highly vulnerable to chronic stress, a common risk factor for mood and anxiety disorders (*19,21*). To molecularly define the hippocampal substrates underlying antidepressant-like effects, we performed droplet-based single nucleus RNA-sequencing (snRNA-seq) of hippocampal cells in mice treated with Cort or Cort + Flx for 5 days or 3 weeks (**Fig. 2A**). Five days of Flx treatment was chosen to define the early events preceding behavioral effects (**Fig. 1B-C**). We recovered 119, 346 nuclei across all conditions and identified all major neuronal and glial subtypes in the hippocampus for downstream analyses (**Fig. 2B-C**, and **Fig. S1A-D**).

Unsupervised clustering analysis revealed a distinct transcriptomic shift between Cort and Cort + Flx (3wks) groups, which primarily mapped onto DG granule cells and was not present after 5 days of Flx (**Fig. 2D-E**). To quantify the level of transcriptomic reprogramming post-Flx, we measured the number of differentially expressed genes (DEGs) between Cort and Cort + Flx groups for each cell type (**Fig. 2F**). All cell types were downsampled to equal numbers of nuclei (588 nuclei per cell type, see *Methods*). After 5 days of Flx treatment, apart from microglia, we found little transcriptional activity. This was consistent with the lack of behavioral effects at this timepoint (**Fig. 1B-C**) and raises the possibility that microglia could play a causal role in the chronic Flx response. Whereas a microglia response dominated at 5 days of Flx treatment, neuronal responses became more prominent after 3 weeks (**Fig. 2F**). Consistent with the transcriptomic shift observed in our unsupervised clustering analysis (**Fig. 1D-E**), DG granule cells produced the largest number of DEGs after 3 weeks of Flx, an effect that was at least ~4-fold greater than any other neuronal cell type. Altogether, these results suggest that granule cells in the DG are highly sensitive to the effects of chronic Flx.

The DG contains a heterogeneous population of granule cells comprised of mature neurons generated during development and immature neurons generated from adult neurogenesis. Both cell types are required for the antidepressant-like effects of chronic Flx in rodents (*5,6*), yet how they modify stress-related behaviors after SSRI treatment remains poorly understood. To investigate the molecular responses to Flx, we leveraged the single cell resolution of our approach and subclustered the granule cell population (34,976 nuclei), revealing 3 additional clusters (**Fig. 2G**). Clusters 1 and 2 were identified as mature granule cells, characterized by expression of *Dock10* and absence of the immature granule cell marker *Igfbpl1* (*22*). Cluster 3 corresponded to immature granule cells (*Igfbpl1*+; **Fig. 2H**). In Cort and Cort + Flx (5d) groups, mature granule cells primarily overlapped with cluster 2, suggesting minimal transcriptional responses at this timepoint (**Fig. 2I-J**). However, in the Cort + Flx (3 wks) group, mature granule cells primarily overlapped with cluster 1, indicating a shift towards a distinct cellular state. In contrast, immature granule cells remained transcriptomically stable across conditions but expanded in number ~4-fold after 3 weeks of Flx, consistent with previous findings that SSRIs enhance hippocampal neurogenesis (*23*). Overall, we found that transcriptional changes in granule cells were primarily driven by mature neurons, which accounted for 85.5% of DEGs in the granule cell population after 3 weeks of Flx (**Fig. 2F**). These results suggest that Flx induces a selective and time-dependent transcriptomic reprogramming in mature granule cells of the DG.

Fluoxetine reactivates a developmental-like plasticity program

To further investigate the unique responses to Flx in mature granule cells, we ranked DEGs between Cort and Cort + Flx (3 wks) groups (**Fig. 3A**). In Flx-treated mice, mature granule cells upregulated genes associated with synaptic transmission and remodeling (**Fig. 3B**), including many presynaptic machinery genes (*Nrxn3*, *Sv2c*, and *Syn3*) and downregulation of negative regulators of mossy fiber synaptogenesis (*Sema5a*, *Ablim3*, and *Pten*; (*24–26*)). Interestingly, we also found downregulation of the mature neuronal marker *Calb1* (Calbindin), consistent with previous studies proposing that mature granule cells can undergo dematuration (*27*). Consistent with bulk transcriptomic approaches (*28*), we found increased expression of genes related to neurotrophic signaling (*Bdnf*, *Ntrk2*, and *Acvr1*). Gene ontology analysis revealed novel Flx-driven pathways in mature granule cells, including Developmental Biology (*Sox11*, *Bdnf*, *Nfix*, and *Sema3e*) and Extracellular Matrix Organization (*Adamts6*, *Ptprn*, and *Large1*; **Fig. 3A-B**).

Critical periods are developmental windows of heightened experience-dependent refinement of neural circuits that typically close during late adolescence (*8*). In adult mice, Flx can reactivate features of critical period plasticity, such as ocular dominance plasticity and enhanced axon regeneration (*16–18*). However, the mechanisms underlying these processes and their connection to antidepressant effects in the hippocampus remain poorly understood. Given Flx's ability to induce critical period-like plasticity, we investigated whether it also reactivates a neurodevelopmental transcriptional program. We analyzed a scRNA-seq dataset of the DG across developmental stages (*29*) and compared DEGs between granule cells from juvenile (P5) versus adult (P132) mice. We then generated a 'juvenile granule cell score' reflecting expression of the top 100 genes upregulated in juvenile granule cells (**Fig. 3C**, and **Fig. S3A-B**). As expected, immature granule cells derived from adult neurogenesis closely resembled juvenile granule cells (**Fig. 3D-E**), consistent with evidence that adult neurogenesis recapitulates features of neurodevelopment (*30*). Surprisingly, we also found an increased 'juvenile granule cell score' in mature granule cells specifically in the Cort + Flx (3 wks) group, but not after 5 days of Flx (**Fig. 3D-E**). Consistent with this, mature granule cells in the Cort + Flx (3 wks) group also showed similarity to two conditions which display a developmental-like state: adult hippocampal neurogenesis and regenerating spinal cord neurons (**Fig. S3C-E**) (*30–33*). The increased resemblance of mature granule cells to a developmental-like state was further confirmed in an independent snRNA-seq dataset of hippocampal neurons following treatment with Flx (3 weeks) or electroconvulsive shock (ECS), a distinct intervention that also produced anxiolytic and antidepressant-like effects (**Fig. S4**). These data indicate that two antidepressant modalities (SSRI and ECS) can reinstate a latent neurodevelopmental transcriptional program in mature granule cells, distinct from their known effects on adult neurogenesis.

We next assessed how reactivation of this developmental program could impact DG function. *Sox11* is a transcription factor that directly promotes an immature neuronal state (*31,34*) and is among the top genes distinguishing juvenile from adult granule cells in both mice and humans (**Fig. S3B**) (*35*). Both *Sox11* and *Bdnf*, a neurotrophin essential for neurodevelopment and synaptic plasticity (*36,37*), were upregulated in mature granule cells following chronic Flx treatment (**Fig. 3F**, and **Fig. S3F**). SOX11 was expressed in 95.5% of PROX1+ granule cells in juvenile mice, but only 7.6% in adults (**Fig. 3G-H**). In control conditions, most SOX11+ granule cells in adults corresponded to DCX+ immature neurons arising from adult neurogenesis (**Fig. 3I**, and **Fig. S3G**). After 3 weeks of Flx treatment, 52.9% of mature granule cells (PROX1+ DCX-) reactivated SOX11, an effect not observed after 5 days of treatment (**Fig. 3I-J**). Interestingly, SOX11 reactivation was primarily observed in the outer granule cell layer, which is largely occupied by embryonically generated neurons and distinct from the inner layer, where adult neurogenesis occurs (*38*). Consistent with the developmental pattern of Sox11 expression,

Bdnf levels were significantly higher in juvenile granule cells compared to adults, and 3 weeks of Flx treatment also increased *Bdnf* expression in mature granule cells (**Fig. 3K-N**). In the hippocampus, BDNF was highly concentrated in the mossy fiber pathway–the axonal projections of DG granule cells–where it co-localized with ZNT3, a marker of mossy fiber terminals (**Fig. 3O**). Three weeks of Flx treatment significantly increased mossy fiber BDNF levels (**Fig. 3P-Q**). This was consistent with the observed upregulation of presynaptic machinery genes, including an increase in SV2C+ mossy terminals (**Fig. 3A**, and **Fig. S3H-J**). To determine if reactivating a developmental-like program was linked to structural plasticity, we generated a reporter line with sparse labeling of mossy terminals (*Prox1*$^{creER/+}$; *Rosa26*$^{tdTomato/+}$) and identified the two major terminal types: large mossy terminals and *en passant* varicosities (**Fig. 3R**) (*39*). Chronic Flx treatment increased both the number of mossy terminals and the size of these two bouton subtypes (**Fig. 3S-T**). Altogether, these findings reveal a molecular mechanism by which Flx rejuvenates mature granule cells in the DG, an effect distinct from its role in augmenting adult hippocampal neurogenesis.

Developmental plasticity is reactivated under physiological conditions

Reactivation of developmental pathways is a fundamental mechanism underlying various physiological functions, such as tissue regeneration (*30–33,40*). To investigate whether reinstatement of a developmental program in mature granule cells occurs under normal environmental conditions, we analyzed a snRNA-seq dataset of hippocampal nuclei from mice exposed to two months of environmental enrichment (*41*). In enriched mice, we observed increased expression of both *Sox11* and a 'juvenile granule cell score' in mature granule cells (**Fig. S5**). These findings suggest that reactivating developmental plasticity in mature granule cells is a common mechanism that is recruited during both environmental enrichment and antidepressant treatment.

Turnover of extracellular matrix induces developmental-like plasticity and mitigates stress-induced fear generalization

The extracellular matrix (ECM) is a complex glycoprotein network that stabilizes synapses and restricts plasticity in the mature brain. Perineuronal nets (PNNs), specialized ECM structures encasing neurons, play a key role in closing critical periods towards the end of neurodevelopment (*8,42*). Removal of PNNs and other ECM structures in the adult brain can reactivate features of critical period plasticity, similar to the effects of chronic Flx (*13–15*). Emerging evidence suggests that the ECM is a dynamic regulator of neural plasticity in the adult brain, shaped by processes such as localized release of ECM proteinases and microglia-mediated phagocytosis (*42–45*). Our findings indicate that Flx influences ECM organization pathways in mature granule cells, including upregulation of genes encoding ECM proteinases like ADAMTS6 and downregulation of genes encoding core ECM components like TENASCIN-R (*Tnr*; **Fig. 3A-B**).

To investigate whether ECM structures gate developmental-like plasticity in the hippocampus, we first examined the ECM landscape. Using the lectin *wisteria floribunda agglutinin* (WFA), which binds ECM glycoproteins, we identified WFA-expressing PNNs and an abundance of non-PNN structures (**Fig. 4A**). While PNNs are well-studied, other ECM structures in the brain remain poorly understood. WFA levels were highest in CA2 and notably

elevated in the DG hilus, which is densely occupied by mossy fiber terminals (**Fig. 4B**). In the hilus, WFA formed net-like structures surrounding axon terminals, which we refer to as "perisynaptic nets" (PSNs) to distinguish them from perineuronal nets (PNNs; **Fig. 4C**). The holes in these nets were occupied by ZNT3+ mossy fiber terminals, suggesting a role in shaping the synaptic microenvironment (**Fig. 4D**). PSNs were sparse in juvenile mice compared to adults, and 3 weeks of Flx treatment reduced their density in adulthood, potentially shaping microenvironments more supportive of synaptic plasticity (**Fig. 4E-H**). Consistent with the long timescale of ECM remodeling (*46,47*), no change in net density was observed after 5 days of Flx treatment. These findings reveal that chronic Flx treatment can remodel diffuse ECM structures in the DG, which we termed PSNs to distinguish them from more widely recognized PNNs.

Given that chronic Flx remodeled peri-synaptic ECM and activated a developmental-like plasticity program in the DG, we investigated whether directly removing the ECM could restore this plasticity. While intracranial delivery of the bacterial enzyme Chondroitinase ABC (ChABC) is commonly used to degrade ECM proteoglycans, its effects lack spatial specificity and are transient due to ECM regeneration. To overcome these limitations, we injected an AAV encoding Cre-dependent expression of ChABC into the DG of *Dock10-Cre* mice, enabling cell-specific and constitutive secretion of ChABC from granule cells (**Fig. 4I-J**) (*48*). In Cort-treated mice, removal of ECM in the DG was sufficient to reactivate SOX11 in mature neurons (**Fig. 4K-M**). These data suggest that the ECM directly represses features of developmental plasticity.

We next tested if directly remodeling ECM in the DG was sufficient to produce antidepressant-like responses. In the EPM test, we did not observe a difference in exploration of the anxiogenic open arm between Cort-treated mice injected with AAV-ChABC or AAV-mCherry control virus (**Fig. 4N**). In the NSF test, we observed a trend towards decreased latency to feed in mice injected with AAV-ChABC, although this was not statistically significant (**Fig. 4O**). In the contextual fear generalization task, Cort-treated mice injected with AAV-mCherry control virus were unable to distinguish between the conditioned context A and unconditioned context B at day 14 (**Fig. 4P-R**). This was consistent with the Cort-induced increase in fear memory generalization over time that we previously observed (**Fig. 1E-F**). In contrast, Cort-treated mice injected with AAV-ChABC virus successfully distinguished between contexts A and B at day 14, suggesting that ECM removal can mitigate stress-induced fear generalization. Like Flx-treated mice, removal of ECM around granule cells also reduced global levels of freezing over time. Altogether, these results suggest that ECM remodeling is sufficient to recapitulate the effects of chronic Flx treatment in mitigating stress-related fear generalization.

Discussion

Antidepressants such as SSRIs and electroconvulsive therapy are used to treat mood and anxiety disorders, yet their molecular mechanisms remain poorly understood. This study reveals a mechanism where mature granule cells in the DG function as a cellular substrate for antidepressant-induced plasticity, driven by ECM remodeling and reinstatement of molecular and structural features reminiscent of neurodevelopment.

While adult hippocampal neurogenesis has well-established roles in mediating some antidepressant-like effects (*5,7,49*), our findings reveal that mature granule cells also play a crucial role. It is possible that both mature and immature granule cells work synergistically to shape DG output, with previous studies suggesting that immature granule cells modulate the activity of mature cells (*50,51*). We speculate that in response to antidepressants, mature granule

cells reinstate aspects of developmental plasticity, enhancing their responsiveness to environmental cues and neural influences, including inputs from cortical regions, local interneurons, and immature granule cells.

Our findings also provide evidence that reinstatement of developmental plasticity in mature granule cells is not limited to antidepressant treatment, but also occurs during physiological processes such as environmental enrichment. Enrichment, a paradigm that enhances cognitive function and resilience to stress, led to reactivation of molecular features reminiscent of neurodevelopment, such as *Sox11* expression. This suggests that reactivation of a developmental program in mature granule cells is a fundamental process engaged during both learning-related processes and antidepressant response.

What enables mature granule cells to regain a developmental-like state? The ECM plays a crucial role in stabilizing neural circuits and restricting synapse plasticity in the adult brain *(13–15,43,44*). We identified a novel ECM structure in the DG, termed perisynaptic nets (PSNs), which are far more abundant than the well-characterized perineuronal nets. Chronic Flx treatment reduced PSN density, coinciding with increased expression of ECM-modifying enzymes such as Adamts6, and the transcriptional activation of microglia (**Fig. 2E-F**), which can also regulate ECM dynamics through phagocytosis (*45*). Notably, targeted ECM degradation in the DG was sufficient to reactivate features of developmental plasticity and produced antidepressant-like effects by mitigating fear generalization. These findings suggest that ECM turnover is a crucial regulator of antidepressant-induced plasticity, creating a permissive environment for reactivation of a developmental-like state.

Our findings may provide important insights for understanding antidepressant efficacy in human patients. The ability of fluoxetine and electroconvulsive shock to rejuvenate mature granule cells points to a potential novel mechanism by which antidepressants enhance neural plasticity. While the amount of adult hippocampal neurogenesis in humans remains debated (*52,53*), our results indicate that rejuvenation of mature granule cells–the most abundant cell type in the hippocampus–could play a critical role in the therapeutic effects of SSRIs. Better understanding how neurons can access latent reservoirs of developmental plasticity represents a promising avenue for developing more effective therapeutic strategies for psychiatric and neurological disorders.

References and Notes

1. World Health Organization. Depression and Other Common Mental Disorders. In 2017 [cited 2025 Jan 2]. Available from: https://www.who.int/publications/i/item/depression-global-health-estimates

2. Rush AJ, Trivedi MH, Wisniewski SR, Nierenberg AA, Stewart JW, Warden D, et al. Acute and longer-term outcomes in depressed outpatients requiring one or several treatment steps: a STAR*D report. Am J Psychiatry. 2006 Nov;163(11):1905–17.

3. McKinnon MC, Yucel K, Nazarov A, MacQueen GM. A meta-analysis examining clinical predictors of hippocampal volume in patients with major depressive disorder. J Psychiatry Neurosci. 2009 Jan;34(1):41–54.

4. Boldrini M, Santiago AN, Hen R, Dwork AJ, Rosoklija GB, Tamir H, et al. Hippocampal granule neuron number and dentate gyrus volume in antidepressant-treated and untreated major depression. Neuropsychopharmacology : official publication of the American College of Neuropsychopharmacology. 2013 May;38(6):1068–77.

5. Santarelli L, Saxe M, Gross C, Surget A, Battaglia F, Dulawa S, et al. Requirement of Hippocampal Neurogenesis for the Behavioral Effects of Antidepressants. Science. 2003 Aug 8;301(5634):805–9.

6. Samuels BA, Anacker C, Hu A, Levinstein MR, Pickenhagen A, Tsetsenis T, et al. 5-HT1A receptors on mature dentate gyrus granule cells are critical for the antidepressant response. Nature Neuroscience. 2015 Nov 1;18(11):1606–16.

7. David DJ, Samuels BA, Rainer Q, Wang JW, Marsteller D, Mendez I, et al. Neurogenesis-Dependent and -Independent Effects of Fluoxetine in an Animal Model of Anxiety/Depression. Neuron. 2009 May 28;62(4):479–93.

8. Hensch TK. Critical period regulation. Annu Rev Neurosci. 2004;27:549–79.

9. Riga D, Kramvis I, Koskinen MK, van Bokhoven P, van der Harst JE, Heistek TS, et al. Hippocampal extracellular matrix alterations contribute to cognitive impairment associated with a chronic depressive-like state in rats. Sci Transl Med. 2017 Dec 20;9(421):eaai8753.

10. Alaiyed S, McCann M, Mahajan G, Rajkowska G, Stockmeier CA, Kellar KJ, et al. Venlafaxine Stimulates an MMP-9-Dependent Increase in Excitatory/Inhibitory Balance in a Stress Model of Depression. J Neurosci. 2020 May 27;40(22):4418–31.

11. Nardou R, Sawyer E, Song YJ, Wilkinson M, Padovan-Hernandez Y, de Deus JL, et al. Psychedelics reopen the social reward learning critical period. Nature. 2023 Jun;618(7966):790–8.

12. Mukhopadhyay S, Chatterjee A, Tiwari P, Ghai U, Vaidya VA. Postnatal Fluoxetine Treatment Alters Perineuronal Net Formation and Maintenance in the Hippocampus. eNeuro. 2021;8(2):ENEURO.0424-20.2021.

13. Pizzorusso T, Medini P, Berardi N, Chierzi S, Fawcett JW, Maffei L. Reactivation of ocular dominance plasticity in the adult visual cortex. Science. 2002 Nov 8;298(5596):1248–51.

14. Gogolla N, Caroni P, Lüthi A, Herry C. Perineuronal nets protect fear memories from erasure. Science. 2009 Sep 4;325(5945):1258–61.

15. Moon LD, Asher RA, Rhodes KE, Fawcett JW. Regeneration of CNS axons back to their target following treatment of adult rat brain with chondroitinase ABC. Nat Neurosci. 2001 May;4(5):465–6.

16. Karpova NN, Pickenhagen A, Lindholm J, Tiraboschi E, Kulesskaya N, Ágústsdóttir A, et al. Fear Erasure in Mice Requires Synergy Between Antidepressant Drugs and Extinction Training. Science. 2011 Dec 23;334(6063):1731–4.

17. Maya Vetencourt JF, Sale A, Viegi A, Baroncelli L, De Pasquale R, O'Leary OF, et al. The antidepressant fluoxetine restores plasticity in the adult visual cortex. Science. 2008 Apr 18;320(5874):385–8.

18. Scali M, Begenisic T, Mainardi M, Milanese M, Bonifacino T, Bonanno G, et al. Fluoxetine treatment promotes functional recovery in a rat model of cervical spinal cord injury. Sci Rep. 2013;3:2217.

19. McEwen BS, Magarinos AM. Stress and hippocampal plasticity: implications for the pathophysiology of affective disorders. Hum Psychopharmacol. 2001 Jan;16(S1):S7–19.

20. LeMoult J, Gotlib IH. Depression: A cognitive perspective. Clin Psychol Rev. 2019 Apr;69:51–66.

21. Leal SL, Tighe SK, Jones CK, Yassa MA. Pattern Separation of Emotional Information in Hippocampal Dentate and CA3. Hippocampus. 2014 Sep;24(9):1146–55.

22. Zhou Y, Su Y, Li S, Kennedy BC, Zhang DY, Bond AM, et al. Molecular landscapes of human hippocampal immature neurons across lifespan. Nature. 2022 Jul;607(7919):527–33.

23. Malberg JE, Eisch AJ, Nestler EJ, Duman RS. Chronic Antidepressant Treatment Increases Neurogenesis in Adult Rat Hippocampus. Journal of Neuroscience [Internet]. 2000 [cited 2017 Aug 14];20(24). Available from: http://www.jneurosci.org/content/20/24/9104?ijkey=b0678ce23159697a43bfec2545c4cff116cef6a4&keytype2=tf_ipsecsha

24. Duan Y, Wang SH, Song J, Mironova Y, Ming G li, Kolodkin AL, et al. Semaphorin 5A inhibits synaptogenesis in early postnatal- and adult-born hippocampal dentate granule cells. Elife. 2014 Oct 14;3:e04390.

25. Guo N, Soden ME, Herber C, Kim MT, Besnard A, Lin P, et al. Dentate granule cell recruitment of feedforward inhibition governs engram maintenance and remote memory generalization. Nature medicine. 2018 May;24(4):438–49.

26. Yonan JM, Steward O. Vector-mediated PTEN deletion in the adult dentate gyrus initiates new growth of granule cell bodies and dendrites and expansion of mossy fiber terminal fields that continues for months. Neurobiol Dis. 2023 Aug;184:106190.

27. Kobayashi K, Ikeda Y, Sakai A, Yamasaki N, Haneda E, Miyakawa T, et al. Reversal of hippocampal neuronal maturation by serotonergic antidepressants. Proceedings of the National Academy of Sciences. 2010 May 4;107(18):8434–9.

28. Rayan NA, Kumar V, Aow J, Rastegar N, Lim MGL, O'Toole N, et al. Integrative multi-omics landscape of fluoxetine action across 27 brain regions reveals global increase in energy metabolism and region-specific chromatin remodelling. Mol Psychiatry. 2022 Nov;27(11):4510–25.

29. Hochgerner H, Zeisel A, Lönnerberg P, Linnarsson S. Conserved properties of dentate gyrus neurogenesis across postnatal development revealed by single-cell RNA sequencing. Nature Neuroscience. 2018 Feb 15;21(2):290–9.

30. Esposito MS, Piatti VC, Laplagne DA, Morgenstern NA, Ferrari CC, Pitossi FJ, et al. Neuronal Differentiation in the Adult Hippocampus Recapitulates Embryonic Development. Journal of Neuroscience. 2005 Nov 2;25(44):10074–86.

31. Rasetto NB, Giacomini D, Berardino AA, Waichman TV, Beckel MS, Di Bella DJ, et al. Transcriptional dynamics orchestrating the development and integration of neurons born in the adult hippocampus. Sci Adv. 10(29):eadp6039.

32. Matson KJE, Russ DE, Kathe C, Hua I, Maric D, Ding Y, et al. Single cell atlas of spinal cord injury in mice reveals a pro-regenerative signature in spinocerebellar neurons. Nat Commun. 2022 Sep 26;13(1):5628.

33. Poplawski GHD, Kawaguchi R, Van Niekerk E, Lu P, Mehta N, Canete P, et al. Injured adult neurons regress to an embryonic transcriptional growth state. Nature. 2020 May;581(7806):77–82.

34. Norsworthy MW, Bei F, Kawaguchi R, Wang Q, Tran NM, Li Y, et al. Sox11 Expression Promotes Regeneration of Some Retinal Ganglion Cell Types but Kills Others. Neuron. 2017 Jun 21;94(6):1112-1120.e4.

35. Ramnauth AD, Tippani M, Divecha HR, Papariello AR, Miller RA, Nelson ED, et al. Spatiotemporal analysis of gene expression in the human dentate gyrus reveals age-associated changes in cellular maturation and neuroinflammation. bioRxiv. 2024 May 6;2023.11.20.567883.

36. Cohen-Cory S, Kidane AH, Shirkey NJ, Marshak S. Brain-derived neurotrophic factor and the development of structural neuronal connectivity. Dev Neurobiol. 2010 Apr;70(5):271–88.

37. Bath KG, Lee FS. Variant BDNF (Val66Met) impact on brain structure and function. Cogn Affect Behav Neurosci. 2006 Mar;6(1):79–85.

38. Erwin SR, Sun W, Copeland M, Lindo S, Spruston N, Cembrowski MS. A Sparse, Spatially Biased Subtype of Mature Granule Cell Dominates Recruitment in Hippocampal-Associated Behaviors. Cell Reports. 2020 Apr 28;31(4):107551.

39. Acsády L, Kamondi A, Sík A, Freund T, Buzsáki G. GABAergic cells are the major postsynaptic targets of mossy fibers in the rat hippocampus. J Neurosci. 1998 May 1;18(9):3386–403.

40. Miao Q, Hill MC, Chen F, Mo Q, Ku AT, Ramos C, et al. SOX11 and SOX4 drive the reactivation of an embryonic gene program during murine wound repair. Nat Commun. 2019 Sep 6;10(1):4042.

41. Pérez RF, Tezanos P, Peñarroya A, González-Ramón A, Urdinguio RG, Gancedo-Verdejo J, et al. A multiomic atlas of the aging hippocampus reveals molecular changes in response to environmental enrichment. Nat Commun. 2024 Jul 16;15(1):5829.

42. Frischknecht R, Gundelfinger ED. The brain's extracellular matrix and its role in synaptic plasticity. Adv Exp Med Biol. 2012;970:153–71.

43. Orlando C, Ster J, Gerber U, Fawcett JW, Raineteau O. Perisynaptic chondroitin sulfate proteoglycans restrict structural plasticity in an integrin-dependent manner. Journal of Neuroscience. 2012 Dec 12;32(50):18009–17.

44. Oray S, Majewska A, Sur M. Dendritic spine dynamics are regulated by monocular deprivation and extracellular matrix degradation. Neuron. 2004 Dec 16;44(6):1021–30.

45. Nguyen PT, Dorman LC, Pan S, Vainchtein ID, Han RT, Nakao-Inoue H, et al. Microglial Remodeling of the Extracellular Matrix Promotes Synapse Plasticity. Cell. 2020 Jul 23;182(2):388-403.e15.

46. Heo S, Diering GH, Na CH, Nirujogi RS, Bachman JL, Pandey A, et al. Identification of long-lived synaptic proteins by proteomic analysis of synaptosome protein turnover. Proc Natl Acad Sci U S A. 2018 Apr 17;115(16):E3827–36.

47. Tsien RY. Very long-term memories may be stored in the pattern of holes in the perineuronal net. Proc Natl Acad Sci U S A. 2013 Jul 23;110(30):12456–61.

48. Carstens KE, Gloss BR, Alexander GM, Dudek SM. Modified adeno-associated virus targets the bacterial enzyme chondroitinase ABC to select mouse neuronal populations in vivo using the Cre-LoxP system. Eur J Neurosci. 2021 Jun;53(12):4005–15.

49. Santiago AN, Nguyen P, Castello-Saval J, Chung HM, Luna VM, Hen R, et al. Effects of electroconvulsive shock on the function, circuitry, and transcriptome of dentate gyrus granule neurons [Internet]. bioRxiv; 2024 [cited 2025 Jan 6]. p. 2024.03.01.583011. Available from: https://www.biorxiv.org/content/10.1101/2024.03.01.583011v2

50. Anacker C, Luna VM, Stevens GS, Millette A, Shores R, Jimenez JC, et al. Hippocampal neurogenesis confers stress resilience by inhibiting the ventral dentate gyrus. Nature. 2018 Jul 27;559(7712):98–102.

51. Luna VM, Anacker C, Burghardt NS, Khandaker H, Andreu V, Millette A, et al. Adult-born hippocampal neurons bidirectionally modulate entorhinal inputs into the dentate gyrus. Science. 2019;364(6440):578–83.

52. Sorrells SF, Paredes MF, Cebrian-Silla A, Sandoval K, Qi D, Kelley KW, et al. Human hippocampal neurogenesis drops sharply in children to undetectable levels in adults. Nature. 2018 Mar 7;555(7696):377–81.

53. Tosoni G, Ayyildiz D, Bryois J, Macnair W, Fitzsimons CP, Lucassen PJ, et al. Mapping human adult hippocampal neurogenesis with single-cell transcriptomics: Reconciling controversy or fueling the debate? Neuron. 2023 Jun 7;111(11):1714-1731.e3.

54. Kohara K, Pignatelli M, Rivest AJ, Jung HY, Kitamura T, Suh J, et al. Cell type-specific genetic and optogenetic tools reveal novel hippocampal CA2 circuits. Nat Neurosci. 2014 Feb;17(2):269–79.

55. Dulawa SC, Holick KA, Gundersen B, Hen R. Effects of chronic fluoxetine in animal models of anxiety and depression. Neuropsychopharmacology. 2004 Jul;29(7):1321–30.

56. Pennington ZT, Dong Z, Feng Y, Vetere LM, Page-Harley L, Shuman T, et al. ezTrack: An open-source video analysis pipeline for the investigation of animal behavior. Sci Rep. 2019 Dec 27;9(1):19979.

57. Stuart T, Butler A, Hoffman P, Hafemeister C, Papalexi E, Mauck WM, et al. Comprehensive Integration of Single-Cell Data. Cell. 2019 Jun 13;177(7):1888-1902.e21.

58. Cembrowski MS, Wang L, Sugino K, Shields BC, Spruston N. Hipposeq: a comprehensive RNA-seq database of gene expression in hippocampal principal neurons. eLife. 2016 Apr 26;5:e14997.

59. Iwano T, Masuda A, Kiyonari H, Enomoto H, Matsuzaki F. Prox1 postmitotically defines dentate gyrus cells by specifying granule cell identity over CA3 pyramidal cell fate in the hippocampus. Development [Internet]. 2012 [cited 2016 Oct 19];139(16). Available from: http://dev.biologists.org/content/139/16/3051

60. Zappia L, Oshlack A. Clustering trees: a visualization for evaluating clusterings at multiple resolutions. Gigascience. 2018 Jul 1;7(7):giy083.

61. Zhou Y, Zhou B, Pache L, Chang M, Khodabakhshi AH, Tanaseichuk O, et al. Metascape provides a biologist-oriented resource for the analysis of systems-level datasets. Nat Commun. 2019 Apr 3;10(1):1523.

62. Marsh S, Salmon M, Hoffman P, kew24. samuel-marsh/scCustomize: Version 3.0.1 [Internet]. Zenodo; 2024 [cited 2025 Feb 11]. Available from: https://zenodo.org/records/14529706

Acknowledgments: We are grateful for S. Schacher and W. Chang for helpful comments on this manuscript. We thank S. Tonegawa for sharing the Dock10-cre mouse strain and S. Dudek for sharing the AAV-ChABC and AAV-mCherry viral reagents. We are grateful for J. Castello-Saval and D. Rivera for assistance with electroconvulsive shock and tissue preparation. We thank the Single Cell Analysis Core of the Columbia University Sulzberger Genome Center under the leadership of Dr. Erin Bush and the Columbia Stem Cell Initiative Flow Cytometry core facility at Columbia University Irving Medical Center under the leadership of Dr. Michael Kissner.

Funding: P.T.N. is a Fellow of The Jane Coffin Childs Fund for Medical Research. This work was supported by National Institutes of Health grants to R.H. (R01 MH083862 and R01 AG043688). R.H. was also supported by the Hope for Depression Research Foundation (RGA-13-003).

Author contributions: Conceptualization: PTN, RH; Methodology: PTN, YX, RH; Investigation: PTN, ST, ES, YS; Visualization: PTN, RH; Funding acquisition: PTN, CL, GFT, RH; Project administration: PTN, RH; Supervision: RH; Writing – original draft: PTN, RH; Writing – review & editing: all authors

Competing interests: Authors declare that they have no competing interests.

Data and materials availability: All data needed to evaluate the conclusions in this paper are present in the paper or the supplementary materials. All mouse strains were obtained from Jackson Laboratories except for Dock10-cre line, which was a gift from S. Tonegawa. Viral reagents used in this study were a gift from S. Dudek. Single nuclei RNA-seq data are available through Gene Expression Omnibus (GEO) accession #GSE289328 and #GSE289329.

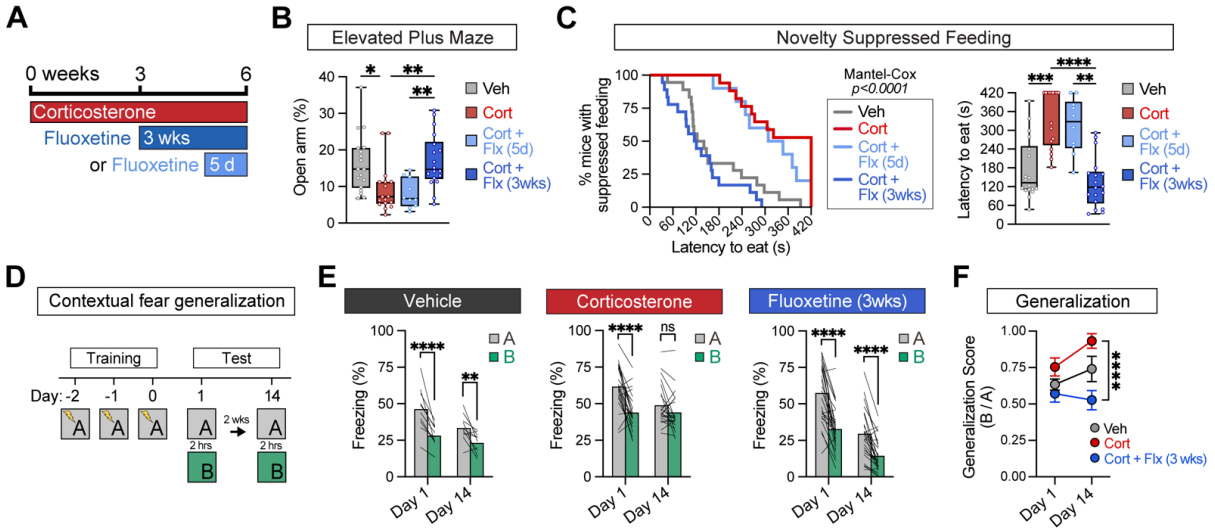

Fig. 1. Fluoxetine mitigates stress-induced anxiety and fear generalization. (**A**) Pharmacological approach. Corticosterone (35 ug/mL) and Fluoxetine (160 ug/mL) were delivered in drinking water. (**B**) Time spent in the open arm of the EPM per mouse (One-way ANOVA, Tukey's multiple comparisons test, n=18 (Veh), 17 (Cort), 10 (Flx 5d), 18 (Flx 3wks)). (**C**) Latency to feed in NSF per mouse shown as survival curve (left; Log-rank Mantel-Cox test, $\chi 2=39.21$, $p<0.0001$) and box plot (right; Kruskal-Wallis test, Dunn's multiple comparisons test, n= same as (B)). (**D**) Schematic of contextual fear generalization assay. (**E**) Freezing in the fear conditioned context A versus unconditioned context B at 1 and 14 days post-training for Veh, Cort, and Cort + Flx (3wks) groups (Two-way repeated measures ANOVA, Sidak's post hoc tests, n=10 (Veh), 22 (Cort), 25 (Flx 3wks)). Lines connect paired data for each mouse. (**F**) Generalization scores at 1 and 14 days calculated as the freezing time in context B divided by context A (Two-way repeated measures ANOVA, Tukey's multiple comparisons tests). Data = mean ± SD. *$p < 0.05$; **$p < 0.01$; ***$p < 0.001$; ****$p < 0.0001$.

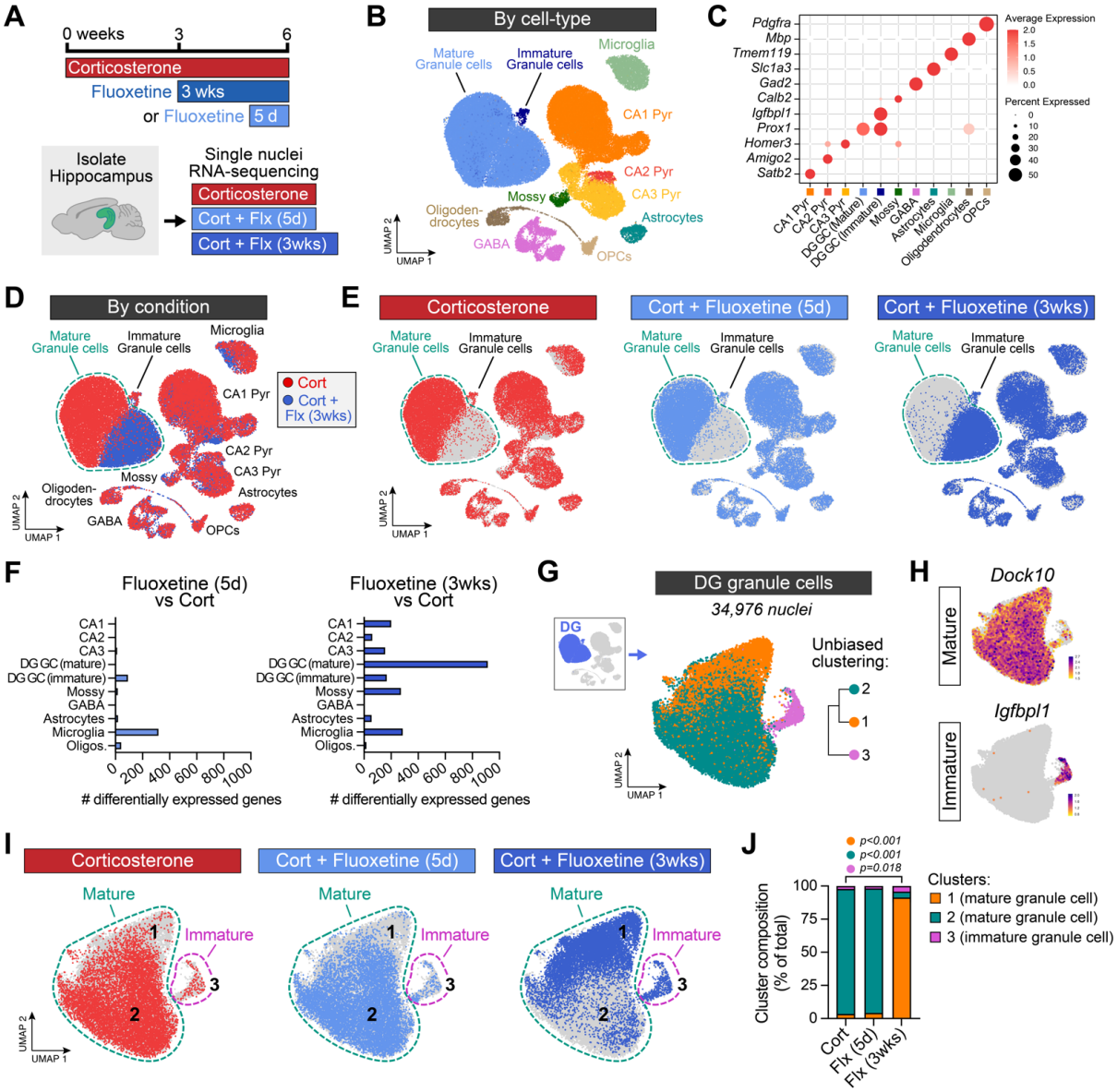

Fig. 2. Transcriptomic reprogramming in mature dentate granule cells after fluoxetine treatment. (**A**) Pharmacological approach for downstream snRNA-seq of hippocampal cells (n=3 mice per condition). (**B**) Unsupervised clustering (uniform manifold approximation and projection (UMAP)) of 119,346 single nuclei transcriptomic profiles labeled by cell type. (**C**) Expression of cell type-specific marker genes for major neuronal and glial populations. See Fig. S2D for additional marker genes. (**D**) Nuclei from Corticosterone + Fluoxetine (Cort + Flx) group (blue) overlaid with nuclei from Cort alone (red). (**E**) Nuclei highlighted by condition. (**F**) Number of differentially expressed genes (DEGs) between Cort and Cort + Flx groups for each cell type. Each cell type was downsampled to 588 nuclei for all analyses. (**G**) Subclustering of 34,976 dentate granule cells from (B). (**H**) Expression of maturation-related marker genes in granule cells. (**I**) Granule cell nuclei highlighted by condition. (**J**) Quantification of granule cell cluster composition from (G) by treatment condition (n=3 mice per condition).

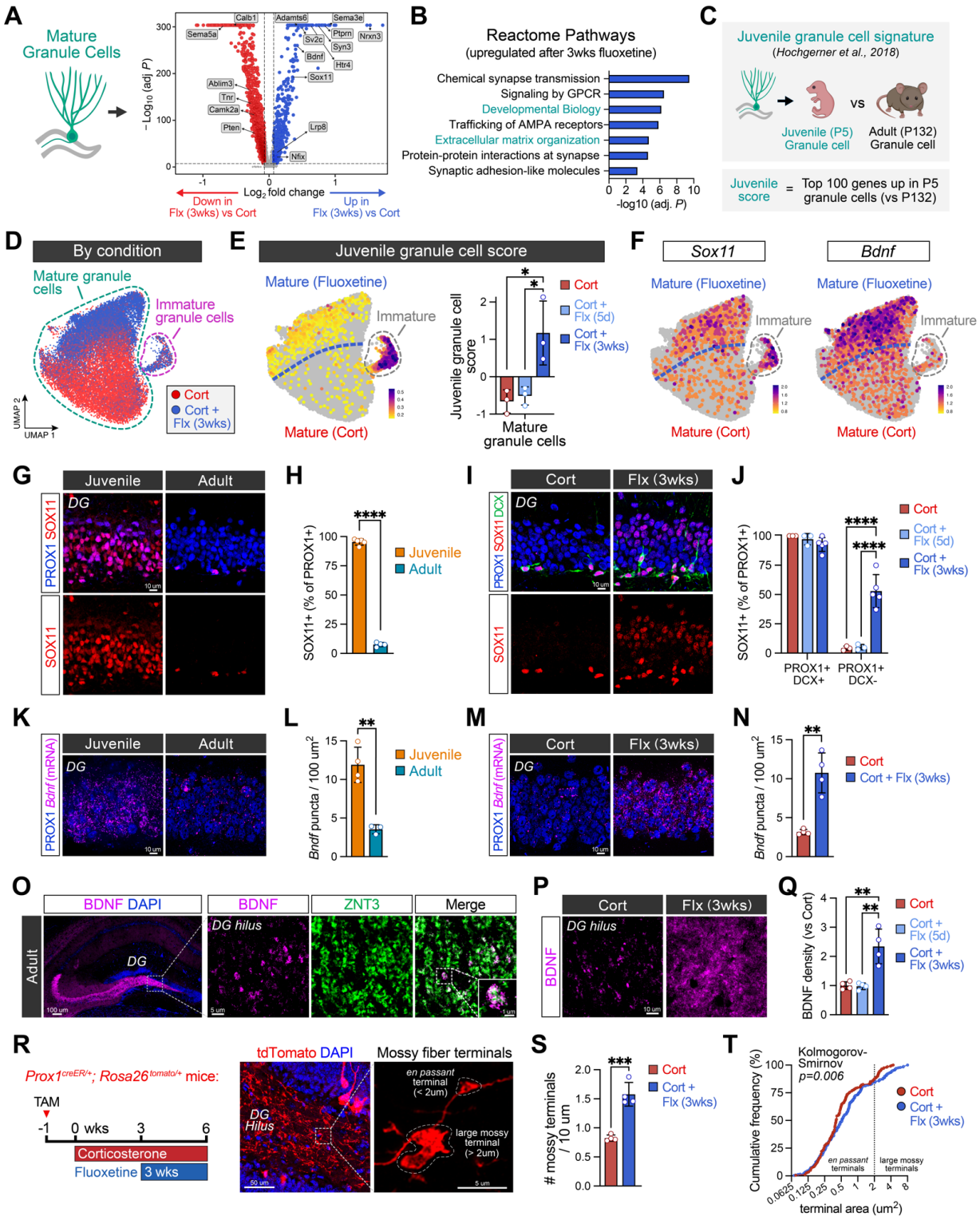

Fig. 3. Fluoxetine reactivates a developmental-like plasticity program in mature granule cells. (**A**) Volcano plot of differentially expressed genes between mature granule cells from Cort and Cort + Flx (3wks) groups. (**B**) Top gene ontology terms for upregulated genes in (A). (**C**) Juvenile granule cell score defined as the top 100 genes upregulated in P5 granule cells versus P132 granule cells. Dataset from (*29*); see also Fig. S3A-B. (**D**) Transcriptomic profiles of dentate granule cells colored by treatment condition (Cort = red, Cort + Flx (3wks) = blue) and cell type (Mature = green outline, Immature = magenta outline). (**E**) Feature plot showing average expression of 'juvenile granule cell score' (left) and z-scores in

mature granule cells per mouse (right; One-way ANOVA, Tukey's multiple comparisons test, n=3 mice/group). (**F**) Expression of *Sox11* and *Bdnf* in granule cells. (**G**) SOX11 protein expression in the DG of juvenile (P10) and adult (~P120) mice. PROX1 marks granule cell neurons. (**H**) Quantification of SOX11+ granule cells per mouse (t-test, n= 5 (juvenile), 4 (adult)). (**I**) SOX11 protein expression in the DG of adult mice treated with Cort or Cort + Flx (3wks). PROX1 marks granule cells, DCX marks immature granule cells. (**J**) Quantification of SOX11+ in mature (PROX1+ DCX-) and immature (PROX1+ DCX+) granule cells per mouse (One-way ANOVA, Tukey's multiple comparisons test, n=3 (Cort), 3 (Cort + Flx 5d), 5 (Cort + Flx 3wks)). (**K**) *Bdnf* mRNA expression in the DG of juvenile (P10) and adult (~P120) mice. (**L**) Quantification of *Bdnf* mRNA in the DG per mouse (t-test, n= 4 (juvenile), 3 (adult)). (**M**) *Bdnf* mRNA expression in the DG of adult mice treated with Cort or Cort + Flx (3wks). (**N**) Quantification of *Bdnf* mRNA in the DG per mouse (t-test, n= 4 (Cort), 4 (Cort + Flx 3wks)). (**O**) Representative image of BDNF protein expression in the hippocampus. Inset shows higher magnifications of BDNF overlapped with ZNT+ mossy fiber terminals and a single mossy terminal. (**P**) BDNF protein levels in the hilar mossy fiber pathway of adult mice treated with Cort or Cort + Flx (3wks). (**Q**) Quantification of BDNF protein levels in the hilar mossy fiber pathway per mouse (One-way ANOVA, Tukey's multiple comparisons test, n=4 mice/group). (**R**) Schematic for genetic and pharmacological approach to sparsely label mossy fiber terminals (left) and representative images of mossy terminals (right). (**S**) Quantification of mossy fiber terminal numbers per mouse in adult mice treated with Cort or Cort + Flx (3wks) (t-test, n= 4 mice/group). (**T**) Quantification of mossy fiber terminal area as cumulative distribution in adult mice treated with Cort or Cort + Flx (3wks) (Kolmogorov-Smirnov test, n= 200 terminals (Cort), 245 (Cort + Flx 3wks)). Data = mean ± SD. *$p < 0.05$; **$p < 0.01$; ***$p < 0.001$; ****$p < 0.0001$.

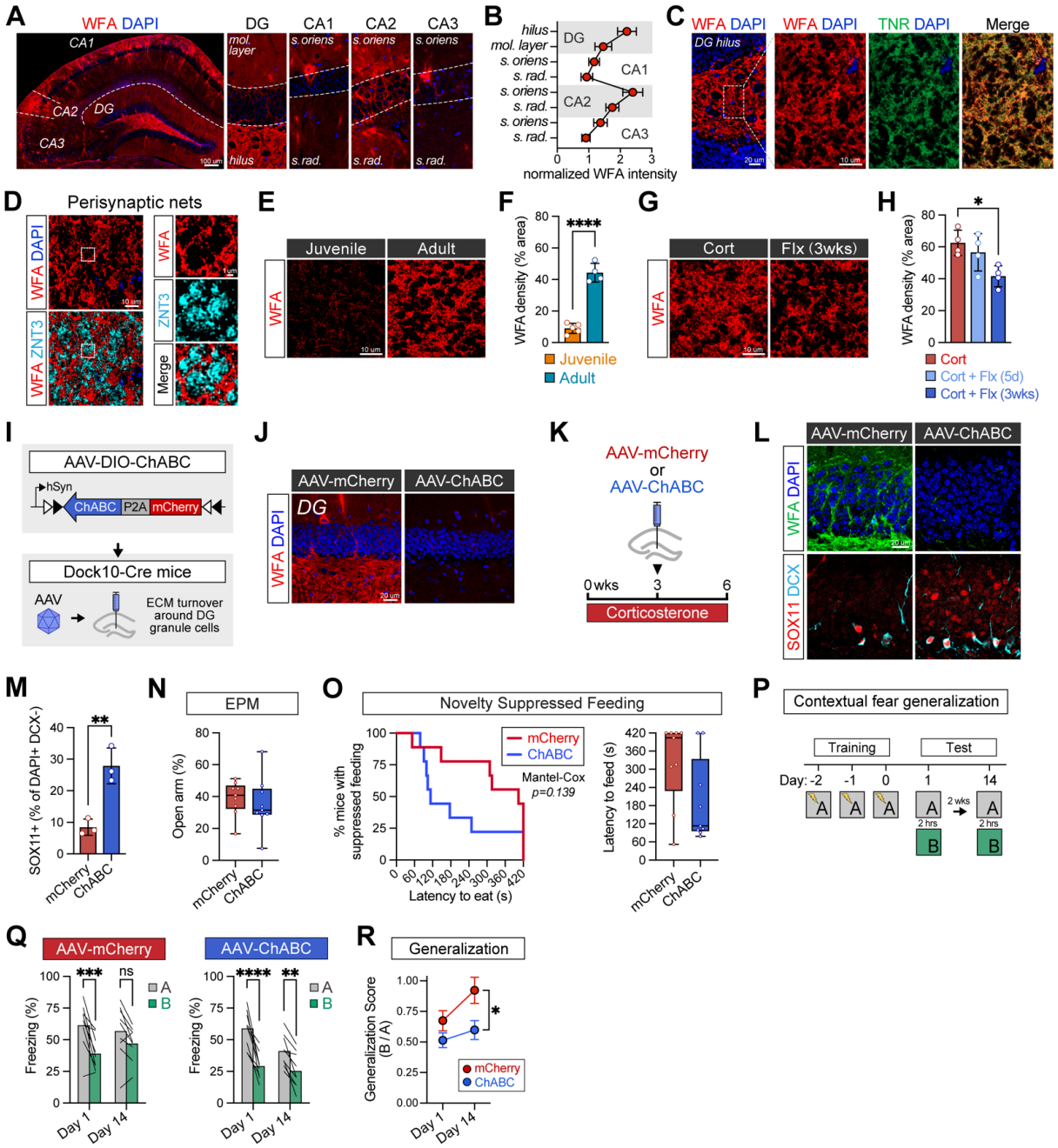

Fig. 4. Turnover of extracellular matrix induces developmental-like plasticity and mitigates stress-induced fear memory generalization. (**A**) Representative image of WFA labeling in the hippocampus. (**B**) Quantification of WFA intensity in hippocampal subregions. (**C**) WFA labeling in the DG forms net-like structures ("perisynaptic nets") that are immunopositive for WFA and Tenascin-R (TNR). (**D**) Holes in perisynaptic nets are filled with ZNT3+ mossy fiber terminals; inset with higher magnification (right). (**E**) WFA staining in the DG hilus of juvenile (P10) and adult (~P120) mice. (**F**) Quantification of WFA levels in DG hilus per mouse (t-test, n= 5 (juvenile), 4 (adult)). (**G**) WFA staining in the DG hilus of adult mice treated with Cort or Cort + Flx (3wks). (**H**) Quantification of WFA levels in DG hilus per mouse (One-way ANOVA, Tukey's multiple comparisons test, n=4 mice/group). (**I**) Schematic of AAV-based strategy for cre-dependent expression of Chondroitinase ABC (ChABC) in dentate granule cells. (**J**) Representative image of WFA levels around DG granule cells in mice injected with AAV-mCherry or AAV-ChABC. (**K**) Paradigm for Cort treatment and AAV-ChABC delivery approach. (**L**) SOX11 expression in dentate granule cells in mice injected with AAV-mCherry or AAV-ChABC. DCX marks

immature granule cells. (**M**) Quantification of SOX11+ granule cells per mouse (t-test, n= 3 (AAV-mCherry), 3 (AAV-ChABC)). (**N**) Time spent in the open arm of the EPM per mouse (t-test, n=9 mice (AAV-mCherry), 9 (AAV-ChABC)). (**O**) Latency to feed in NSF per mouse injected with AAV-mCherry or AAV-ChABC shown as survival curve (left; Log-rank Mantel-Cox test, $\chi 2=2.19$, p=0.139) and box plot (right; Mann–Whitney U test, p=0.124, n= 9 mice/group). (**P**) Schematic of contextual fear generalization assay. (**Q**) Freezing in the fear conditioned context A versus unconditioned context B at 1 and 14 days post-training for mice injected with AAV-mCherry or AAV-ChABC (Two-way repeated measures ANOVA, Sidak's post hoc tests, n=9 mice/group). Lines connect paired data for each mouse. (**R**) Generalization scores at 1 and 14 days calculated as the freezing time in context B divided by context A (Two-way repeated measures ANOVA, Tukey's multiple comparisons tests). Data = mean ± SD. *$p < 0.05$; **$p < 0.01$; ***$p < 0.001$; ****$p < 0.0001$.

Materials and Methods

Animal Studies

All mouse strains were maintained in the New York State Psychiatric Institute specific pathogen-free facility and maintained on a 12-hour light/dark schedule. Mouse protocols were approved by the Institutional Animal Care and Use Committee of Columbia University and the Research Foundation for Mental Hygiene, Inc. and were conducted in accordance with the NIH Guide for the Care and Use of Laboratory Mice. Care was taken to minimize the number of mice used and their suffering.

Littermate controls were used for all experiments when feasible, and all mice were backcrossed > 10 generations on a C57BL/6 background. Male mice were used throughout the manuscript, except where noted otherwise. Dock10-cre mice were a generous gift from Dr. Susumu Tonegawa (54). Prox1-creER (Jax #: 022075) and Rosa26-tomato (Jax #: 007914) mice were purchased through Jackson Labs.

Pharmacological Approach

Corticosterone (Sigma, C2505) was dissolved at a concentration of 35 µg/mL in autoclaved deionized water containing 2 mg/mL beta-cyclodextrin (Chem-Impex, 32075) to improve solubility. The solution was then incubated in a 37°C water bath sonicator for 30 minutes to ensure complete dissolution. Fluoxetine hydrochloride (TCI Chemicals, F0750) was added at a final concentration of 160 ug/mL under the same conditions. Drug solutions were delivered ad libitum in drinking water in opaque bottles to protect from light. Fluoxetine concentrations were previously optimized to achieve brain pharmacokinetics equivalent to 18 mk/kg/day (55).

Behavioral Assays

For contextual fear generalization assays, conditioned fear was elicited by administering a 2 second footshock (0.75 mA) following a 5 minute exposure to an array of contextual cues (conditioning chamber, chamber lights, white noise, scent of anise extract). Fear conditioning involved repeating this protocol for 3 consecutive days. Retrieval of the fear memory was assessed by a three-minute re-exposure of the animal to the conditioning context in the absence of shock where freezing (the cessation of all movement outside of respiration) was interpreted as expression of fear memory. Video recordings were acquired and scored automatically in FreezeFrame (Actimetrics). Mice were habituated to transport and holding in a separate room for at least one hour prior to all conditioning or retrieval sessions and subjected to three days of handling prior to all behavioral tests. For assessment of fear generalization, freezing was measured in a context similar to the conditioning context (context B) 2 hours later, but with the following variations: the chamber fan was turned off, the scent of lemon extract was used instead of anise, and a plastic divider was inserted to make the chamber walls circular and opaque. Freezing in the unconditioned context was tested 2 hours following retrieval testing in the original conditioning context, and animals were rested in a holding room between sessions. Freezing levels were scored using automated motion detection in FreezeView software (Actimetrics).

Anxiety-like behaviors were assessed through 10 minute exposure in the elevated plus maze (EPM) and 7 minute exposure in the novelty suppressed feeding (NSF) arena. In the NSF, mice were food deprived for 24 hours prior to testing. In both tests, the ambient lights were turned off, and lamps were positioned above the open arms in the EPM and at the center of the arena in the NSF, providing targeted illumination of ~150 lux. Video recordings

were acquired using Logitech webcams and OBS Studio software. Time spent in the open arms of the EPM were scored through automated object detection with the open-source ezTrack pipeline (56) and interpreted as anxiety-like behavior. Latency to feed in the NSF, defined as the amount of time a mouse took to first bite the food pellet, was manually scored using video recordings and live observation. To measure the latency to eat in the home cage, each mouse was first placed in a separate holding cage. The mouse was then returned to its home cage, and the time it took for the mouse to bite a food pellet placed at the center of the home cage was measured during a 5 minute exposure. All behavioral testing and analyses were performed blinded to treatment condition and all analyses were conducted using unbiased, automated approaches when possible.

Male C57BL/6 mice (3-4 months old) were used for all behavioral assays, except in the contextual fear generalization assay, where female C57BL/6 littermates were also included. Male mice were initially used based on scientific precedence and amenability with the corticosterone paradigm. See Figure S1. Behavioral experiments were conducted in the mornings, based on local Eastern Standard Time (EST).

Viral Reagents and Stereotaxic Injections

AAV-hSyn-DIO-ChABC-2a-mCherry and AAV-hSyn-DIO-mCherry viral reagents were a generous gift from Dr. Serena Dudek (48) and packaged by the National Institute of Environmental Health Sciences viral vector core facility at titers of 4e12 and 1e13 GC/ml, respectively.

All stereotaxic injections were performed with a Kopf stereotaxic apparatus (David Kopf, Tujunga, CA) with a microdispensing pump (World Precision Instruments) holding a 33g beveled NanoFil needle (World Precision Instruments, NF33BV). Mice were anesthetized with 1.5% isoflurane at an oxygen flow rate of 1L/min, headfixed with a stereotaxic frame, and treated with ophthalmic eye ointment. Fur was shaved and the incision site was sterilized with 70% ethanol and Betadine prior to surgical procedures. Craniotomy was performed using a surgical drill. To induce turnover of extracellular matrix, 1.5uL of AAV-hSyn-DIO-ChABC-2a-mCherry (diluted 1:100) or AAV-hSyn-DIO-mCherry (diluted 1:1000) viral reagents were bilaterally injected into the dentate gyrus (−3mm AP, ±2.4mm ML, and −2.75mm DV) at a rate of 3 nL/sec. Body temperature was maintained throughout surgery using a heating pad. Post-surgery, Carprofen (Covetrus, 059150) was administered as needed by intraperitoneal injection at a concentration of 5 mg/kg.

Single Nuclei RNA Sequencing

Tissue Isolation and Processing:

Whole and intact hippocampi were removed by parting the diencephalon from the cerebral cortex under a dissecting microscope. Excess myelin and meninges were removed. Hippocampi (2 per mouse) were mechanically dissociated using a 2 mL glass tissue homogenizer (Kontes Glassware) on ice using twelve strokes of the tight pestle in 1% BSA-PBS. Nuclei were filtered using a 40 um strainer and pelleted at 300g for 5 minutes at 4°C in a centrifuge. Nuclei were then resuspended in 22% Percoll (GE Healthcare) and centrifuged at 900 g for 20 minutes with acceleration set to 4 and deceleration set to 1 to remove cellular debris. The debris-containing supernatant was removed, and nuclei were washed and resuspended in 1% BSA-PBS before being pelleted at 300 g for 5 minutes at 4°C. Nuclei were resuspended in 1% BSA-PBS prior to loading into the 10x Chromium controller platform. All buffers contained Protector RNase Inhibitor (Roche) at 0.2 U/uL.

Nine samples were prepared corresponding to 3 mice from the Corticosterone group, 3 mice from the Corticosterone + Fluoxetine (5d) group, and 3 mice from the Corticosterone + Fluoxetine (3wks) group. Tissue isolation and library preparations were performed on the same day to mitigate batch effects. This experiment is referred to as Dataset 1 and corresponds to snRNA-seq data in main figures. Dataset 2 (see below) corresponds to data in Fig. S4. Three to four months old C57BL/6 male mice were used for all sequencing studies.

Library Preparation and Sequencing:

Hippocampal nuclei were sequenced using the 10x Single Cell Gene Expression 3' (v3) platform. Approximately 15,000-20,000 intact nuclei from each biological replicate were loaded into each well of Chromium Chip A and combined into droplets with barcoded beads using the Chromium controller according to the manufacturer instructions. Libraries were prepared by the Single Cell Analysis Core of the Columbia University Sulzberger Genome Center following manufacturer instructions and sequenced using an Illumina Novaseq 6000 sequencer. Samples were sequenced to ≥20,000 mean reads per cell with sequencing saturation of ≥35%. Sequenced samples were processed using the Cell Ranger 6.1.2 pipeline and aligned to the mm10-2020-A mouse reference genome. Approximately 140K total cells were recovered prior to quality control processing.

Quality Control and Data Analysis:

Quality control, clustering, and differential expression analysis were conducted in R v4.3.0 using Seurat v4.4.0 (57). Cells with fewer than 1,200 or over 3,600 detected genes/cell, or more than 5% mitochondrial DNA were excluded prior to downstream analyses. Genes that were expressed by fewer than 5 cells in the dataset were also excluded. After filtering for these quality control metrics, we recovered between 9,000-15,000 nuclei for each biological replicate (119,346 total nuclei). See also Figure S2.

Following alignment in Cell Ranger (as described above), molecular counts data were imported into R and analyzed using the Seurat package v4.4.0 (57). Counts data underwent normalization and variance stabilization, regressing out percent mitochondrial RNA and total counts per cell, using the sctransform function in Seurat. The top 6000 most variable genes were used to calculate 50 principal components (PCs), and the top 35 PCs were used for nearest neighbor, UMAP, and clustering. Cell types were identified by expression of known cell type-specific markers (58). We identified rare cell populations, including epithelial cells and pericytes, but these were excluded due to low cell numbers.

For comparison of differentially expressed genes (DEGs) between cell types, each cell type in each biological replicate were downsampled to include the same number of cells (588 nuclei per cell type per mouse). Differential gene expression between treatment conditions were calculated using the MAST test in Seurat (adjusted P value (FDR) < 0.05, log2 fold change > 0.1). Both upregulated and downregulated genes were included in bar plots.

Dentate granule cells were isolated using the granule cell markers *Prox1*, *Dock10*, and *Stxbp6* (58,59), yielding 34,976 nuclei. Notably, oligodendrocyte lineage cells share many granule cell identity marker genes (*Prox1, Dock10, Stxbp6*) and were excluded from the granule cell population by identification with oligodendrocyte (*Mbp, Mog*) and oligodendrocyte progenitor cell (*Pdgfra, Cspg4*) genes. The top 6000 most variable genes in granule cells were used to recalculate PCs, generate UMAP embeddings, and define clusters. Clusters were determined using a resolution of 0.1 using the ClusTree package (60). For granule cell analysis, differential gene expression between treatment conditions were calculated using the MAST test in Seurat. Gene ontology analysis was conducted using Metascape (61) with all genes expressed in dentate granule cells used as background genes. Data visualization was performed using Seurat and the scCustomize package (62).

Comparison with External Single Cell RNA-seq datasets:

External single cell RNA-seq datasets were acquired from Hochgerner et al., (29), Rasetto et al., (31), and Pérez et al., (41). Datasets were downloaded from GEO and processed using Seurat as described above.

For the "Juvenile granule cell score", the top 100 genes enriched in P5 granule cells (relative to P132 granule cells) from Hochgerner et al., (29) were used to generate a gene enrichment score. P5 granule cells were identified based on age and expression of granule cell markers (*Rbfox3, Prox1*, *Dock10*, and *Stxbp6*), and differential gene expression analysis was conducted using the MAST test in Seurat (see also **Fig. S3A-B**). For the "Immature granule cell score", the top 100 genes enriched in 4-week-old adultborn granule cells (relative to 8-week-old adultborn granule cells) from Rasetto et al., (31) were used to generate a gene enrichment score. 4-week-old adultborn granule cells were identified based on metadata provided by Rasetto et al., and DEGs determined as described above (see also **Fig. S3C**). For the "Regeneration associated gene score", gene enrichment scores were generated based on regeneration associated genes (RAGs) provided by Matson et al., (32).

Gene enrichment scores were generated using the AddModuleScore function in Seurat, which calculates the average expression of the query gene list per cell and subtracts the aggregated expression of a control gene set randomly selected from genes with similar expression levels to the query gene list. Enrichment scores were calculated using the entire granule cell population and visualized with Seurat and scCustomize. Z-scores were calculated in Seurat for each biological replicate, using exclusively mature granule cells, and shown in bar plots.

For analyses involving environmental enrichment, snRNA-seq data from hippocampal nuclei were obtained from Pérez et al., (41). DG granule cells were identified based on expression of granule cell markers *Rbfox3, Prox1*, *Dock10*, and *Stxbp6*. The top 3000 most variable genes in granule cells were used to recalculate PCs, generate UMAP embeddings, and define clusters. Volcano plots were generated using DEG analyses from Pérez et al., and "juvenile granule cells scores" were calculated using the same approach as described above.

Dataset 1 and Dataset 2:

The above methods detail isolation and analysis pipelines for Dataset 1. Dataset 2 followed the same procedures as Dataset 1 but includes several key differences: 1) we include 4 groups: vehicle, corticosterone, corticosterone + fluoxetine, and corticosterone + electroconvulsive shock (see "*Electroconvulsive shock (ECS)*" below); 2) hippocampal neuronal nuclei were purified using fluorescence activated nuclei sorting instead of bulk hippocampal homogenate (see "*Flow cytometry*" below).

For Dataset 2, purified neuronal nuclei were sequenced using the 10 Genomics Single Cell Gene Expression 3' platform (v3), following the same protocol and reagents as in Dataset 1. Nuclei hashing was performed to barcode

biological replicates using the CellPlex Multiplexing Oligos (CMO; 10x Genomics, 3' CellPlex Kit Set A, 1000261). Barcoded nuclei were pooled, and approximately 15,000 nuclei were loaded into each of four wells of Chromium Chip A, where they were encapsulated into droplets with barcoded beads using the Chromium Controller. Libraries were prepared by the Single Cell Analysis Core of the Columbia University Sulzberger Genome Center following manufacturer instructions and sequenced using an Illumina Novaseq 6000 sequencer. Samples were sequenced to 45K-60K mean reads per cell with sequencing saturation of ≥33%. Sequenced samples were processed using the Cell Ranger 6.1.2 pipeline and aligned to the mm10-2020-A mouse reference genome. Approximately 70% of all nuclei were successfully assigned to a CMO barcode using the 'cellranger multi' pipeline, resulting in 25,974 recovered nuclei for downstream quality control processing.

For Dataset 2, quality control, clustering, and gene expression analyses were conducted in R v4.3.0 using Seurat v4.4.0, following the same protocol as in Dataset 1. Doublets were identified as nuclei with more than 1 unique CMO barcode, comprising ~5% of total nuclei, and were removed prior to downstream analyses. Cells with fewer than 1600 or over 3600 detected genes/cell, or more than 5% mitochondrial DNA were excluded prior to downstream analyses. Genes that were expressed by fewer than 5 cells in the dataset were also excluded. After filtering for these quality control metrics, we recovered 22,199 total nuclei (5919 vehicle, 6313 Cort, 5323 Cort + Fluoxetine, and 4644 Cort + ECS) See also **Fig. S4**.

Data Availability:

All analysis scripts can be found at https://github.com/pnguyen1003/snRNA-seq-analyses, and original data for Dataset 1 and 2 can be found on GEO with ascension numbers GSE289328 and GSE289329, respectively.

Electroconvulsive Shock (ECS)

Mice were anesthetized with 2% isoflurane using a nose cone with oxygen flow rate of 1 L/min. Electroshocks were delivered to anesthetized mice through ear clipped electrodes at 120 Hz and 50 mA, for a duration of 1 second. Ringers salt solution was applied to the ear prior to shock to improve conductance. Mice received electroconvulsive shock (ECS) treatment once every other day for a total of 10 sessions (21 days) starting after 3 weeks of Corticosterone treatment. For single nuclei RNA-seq experiments in Dataset 2, all groups (vehicle, corticosterone, cort + fluoxetine, cort + ECS) were treated in parallel such that library preparation and sequencing were performed in one batch. The vehicle group received drinking water with 2 mg/mL beta-cyclodextrin (see "*Pharmacological approach*")

Flow Cytometry

For fluorescence activated nuclei sorting (FANS), flow cytometry experiments were performed as previously described (45). Briefly, animals were perfused transcardially with ice-cold 1X PBS and intact hippocampi were isolated under a dissecting microscope where meninges and excess myelin were removed. Hippocampi (2 per mouse) were mechanically homogenized using a 2 mL glass tissue homogenizer (Kontes Glassware) on ice using twelve strokes of the tight pestle in 1% BSA-PBS (Sigma-Aldrich, A3059). Nuclei were filtered using a 40um strainer and then pelleted at 300 g for 5 minutes at 4°C. Nuclei were then resuspended in 22% Percoll (GE Healthcare) in PBS and centrifuged at 900 g for 20 minutes with acceleration set to 4 and deceleration set to 1 to remove cellular debris. Pelleted nuclei were then washed with PBS and incubated in block solution consisting of 1% BSA-PBS for 10 min prior to staining with mouse anti-NeuN antibody conjugated to Alexa Fluor 488 (EMD Millipore, MAB377X) at 1:1000 concentration for 10 min on ice. Cell hashing was performed with CellPlex Multiplexing Oligos (CMO; 10x Genomics, 3' CellPlex Kit Set A, 1000261). CMOs were added to nuclei after primary antibody incubation and samples were incubated at room temperature for an additional 5 min. After 2 additional wash steps with PBS, biological replicates were pooled together prior to fluorescence activated nuclei sorting. All buffers contained Protector RNase Inhibitor (Sigma-Aldrich, 03335399001) at 0.2 U/uL for downstream single cell RNA seq experiments. DAPI (Sigma-Aldrich, D9542) was added to each sample immediately before sorting to identify nuclei. Nuclei were sorted on a Sony MA900 Cell Sorter and gated on forward/side scatter, DAPI, and NeuN (see also **Fig. S4D** for gating strategy). Flow cytometry and cell sorting experiments were performed in the Columbia Stem Cell Initiative Flow Cytometry core facility at Columbia University Irving Medical Center under the leadership of Dr. Michael Kissner. All data analysis was performed using FlowJo software.

Immunohistochemistry and Fluorescence in situ Hybridization (FISH)

For all immunohistochemistry experiments, mice were transcardially perfused with ~10 mL of ice-cold 1X PBS followed by ~10 mL of 4% (weight/volume) paraformaldehyde diluted in PBS. Brains were post-fixed in 4% PFA for a minimum of 4 hours and then transferred to a 30% sucrose solution for a minimum of 2 days. Brains were

then frozen on BFS-40MPA Freezing Stage (Physitemp) and sliced into 40 um thick coronal sections using an HM450 microtome (Epredia).

For immunohistochemistry, brain sections were incubated in a blocking solution consisting of 10% normal goat or donkey serum (Thermo Fisher) and 0.4% Triton (Sigma-Aldrich) diluted in 1X PBS. Primary antibodies were diluted in 3% normal goat or donkey serum in 0.4% Triton and tissue was incubated on a shaker overnight at 4°C. Secondary antibodies were diluted in 3% normal goat or donkey serum and tissue was incubated on a shaker for 2 hours at room temperature. For nuclear labeling, DAPI (Sigma, D9542) was added to secondary antibody incubations during the last 5 minutes at a final concentration of 4 µg/mL. Brain sections were mounted on coverslips with ProLong Glass without DAPI (Thermo Fisher) for high resolution imaging and ProLong Gold (Thermo Fisher) for all other experiments.

For BDNF (Proteintech, 28205-1-AP) immunostaining, antigen retrieval was performed with IHC-Tek Epitope Retrieval Solution (IHC World, IW1100), and brain sections were heated to 95°C for 40 minutes before being washed 3x with PBS and proceeding with the blocking step. Antigen retrieval for SOX11 (Sigma, MABE1929) and PROX1 (R&D Systems, AF2727) immunostaining was performed with the same procedure, but with a 10 minute incubation instead of 40 minutes. Attempts to perform BDNF and SOX11 immunostaining were unsuccessful using the following antibodies, both with and without antigen retrieval: BDNF Santa Cruz Biotech (sc-65514), BDNF Invitrogen (PA5-85730), BDNF Invitrogen (PA5-95183), SOX11 Sigma (ABN105), SOX11 Sigma (MABE1935), and SOX11 Abcam (EPR8192). The following antibodies did not require antigen retrieval: DCX (Synaptic Systems 326014), SV2C (Synaptic Systems 119202), dsRed (Takara 632496), and ZNT3 (Synaptic Systems 197004). All secondary antibodies were purchased from Invitrogen.

FISH experiments were performed using the RNAscope Multiplex Fluorescent Reagent Kit v2 assay (ACD Bio) as described by the manufacturer for fixed-frozen tissue, except tissue was not baked for 30 minutes at 60°C prior to tissue dehydration. Brains were embedded in OCT after 30% sucrose treatment, frozen at −80°C for at least one day, and then sectioned into 15 µm thick coronal slices using a cryostat. The slices were then mounted on coverslips for RNAscope processing. Mouse *Bdnf* RNAscope Probe (ACD Bio, 424821) and TSA Plus Cyanine3 (Perkin Elmer) was used to detect *Bdnf* transcript. For immunohistochemical labeling with antibodies following the RNAscope assay, tissues were incubated with blocking and antibody solutions as described above immediately after developing the HRP-TSA Plus signal and washing four times.

Confocal Microscopy and Image Analysis

Histology slides were imaged on a Zeiss LSM 800 scanning confocal microscopes with Airyscan super-resolution module using a 63x, 40x, or 20x objective.

For quantification of synapse and ECM density (BDNF, SV2c, and WFA), images were acquired using a 63x objective (1.4 NA) with 1x optical zoom (0.04 um pixel size) and superresolution mode in Zen software (Zeiss). AiryScan processing was performed in Zen software and laser power and gain were consistent across all experiments. Images were taken in the hilus of the DG. BDNF, SV2c, and WFA density were quantified using ImageJ by first thresholding each channel and then measuring the area of positive pixels for each corresponding channel. The density (% area) of each channel was calculated by dividing the positive area by the total area. The total area was determined by subtracting the area occupied by large DAPI+ nuclei (likely hilar mossy cells and interneurons) from the total area of the field of view. Regions of interest (ROIs) were drawn around these nuclei, and the ROI task manager in ImageJ was used to calculate the inverse area (i.e. the total area minus the area corresponding to nuclei). Thresholding was held consistent for each image and the experimenter was blinded to sample ID for all quantifications.

For quantification of mossy fiber terminals, images were acquired using superresolution mode in Zen software, as described above, but with a 1.4x optical zoom (0.04 um pixel size). Z stacks were acquired at a step-size set at half the optical section and laser power and gain were consistent across all experiments. Mossy fiber terminal numbers were quantified using ImageJ by measuring a distance of at least 20 um along an axonal branch and then counting boutons. Mossy fiber terminal area was quantified by drawing an ROI around each bouton and calculating the area with ImageJ.

For quantification of *Bdnf* mRNA puncta density, images were acquired using superresolution mode in Zen software, as described above for mossy fiber terminals. Puncta were manually counted using the multi-point tool in ImageJ and normalized by the area of the field of view defined by Prox1 immunopositive signal.

For quantification of SOX11 reactivation, images were acquired using a 40x objective (0.65 NA) with 1x optical zoom (0.08 um pixel size) in Zen software. The proportion of SOX11+ granule cells was determined by manually counting PROX1+ granule cells that were also immunopositive for SOX11.

For quantification of WFA intensity across hippocampal subfields (in contrast to perisynaptic net imaging described above), images were acquired using a 20x objective with 1x optical zoom (0.28 um pixel size) and image

tiling in Zen software. WFA intensity was quantified by drawing an ROI around each hippocampal subfield and measuring its mean fluorescence intensity using ImageJ. This value was then normalized by dividing it by the mean fluorescence intensity of the total field of view, which was static for each hippocampal subfield.

Quantification and Statistical Analysis

GraphPad Prism 10.2.2 was used for most statistical analyses. Statistical tests are as described in text and figure legends. RNA-sequencing data was analyzed in R as described in the methods section above.

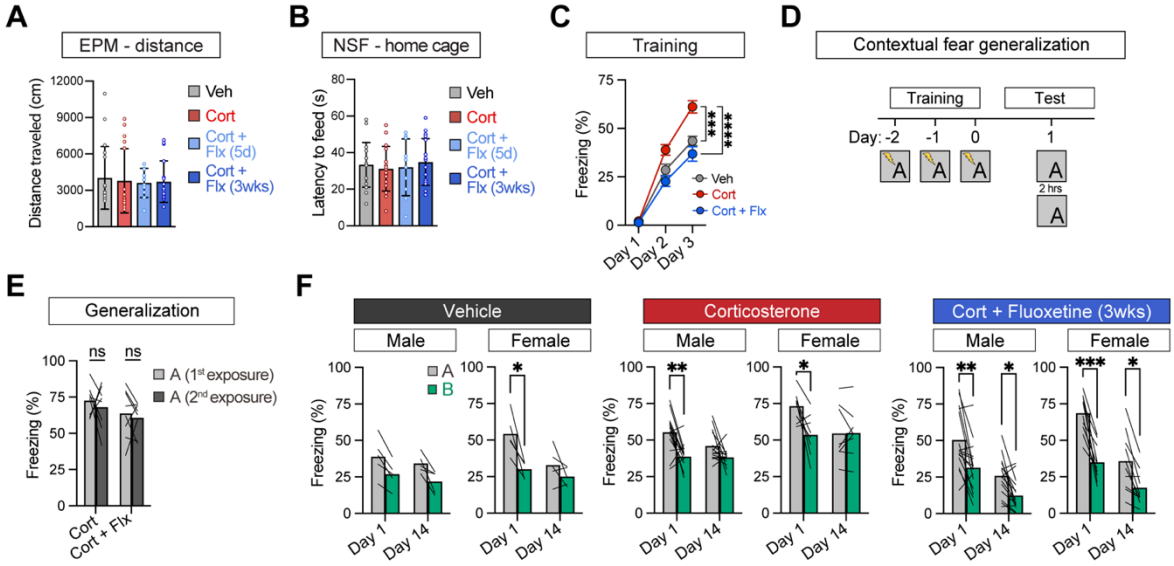

Fig. S1. Additional data pertaining to behavioral studies; related to Figure 1. (**A**) Distance traveled in the EPM per mouse (One-way ANOVA, p= 0.96, n=18 (Veh), 17 (Cort), 10 (Flx 5d), 18 (Flx 3wks)). (**B**) Latency to feed in home cage per mouse (One-way ANOVA, p= 0.85, n= same as (A)). (**C**) Freezing levels during contextual fear conditioning training (Two-way RM ANOVA, day x condition p< 0.0001, Tukey's post-hoc tests, n=10 (Veh), 22 (Cort), 25 (Flx 3wks)). (**D**) Paradigm to assess freezing due to contextual habituation where mice are returned to the same context A. (**E**) Freezing between first and second exposure in context A (Two-way RM ANOVA, Sidak's post-hoc tests, n=8 mice/group). (**F**) Freezing in context A versus B at 1 and 14 days post-training by sex for each group (Two-way RM ANOVA, Sidak's post-hoc tests, n=5 (Veh-Male), 5 (Veh-Female), 14 (Cort-Male), 8 (Cort-Female), 15 (Flx-Male), 10 (Flx-Female)). Lines connect paired data for each mouse. *$p < 0.05$; **$p < 0.01$; ***$p < 0.001$; ****$p < 0.0001$.

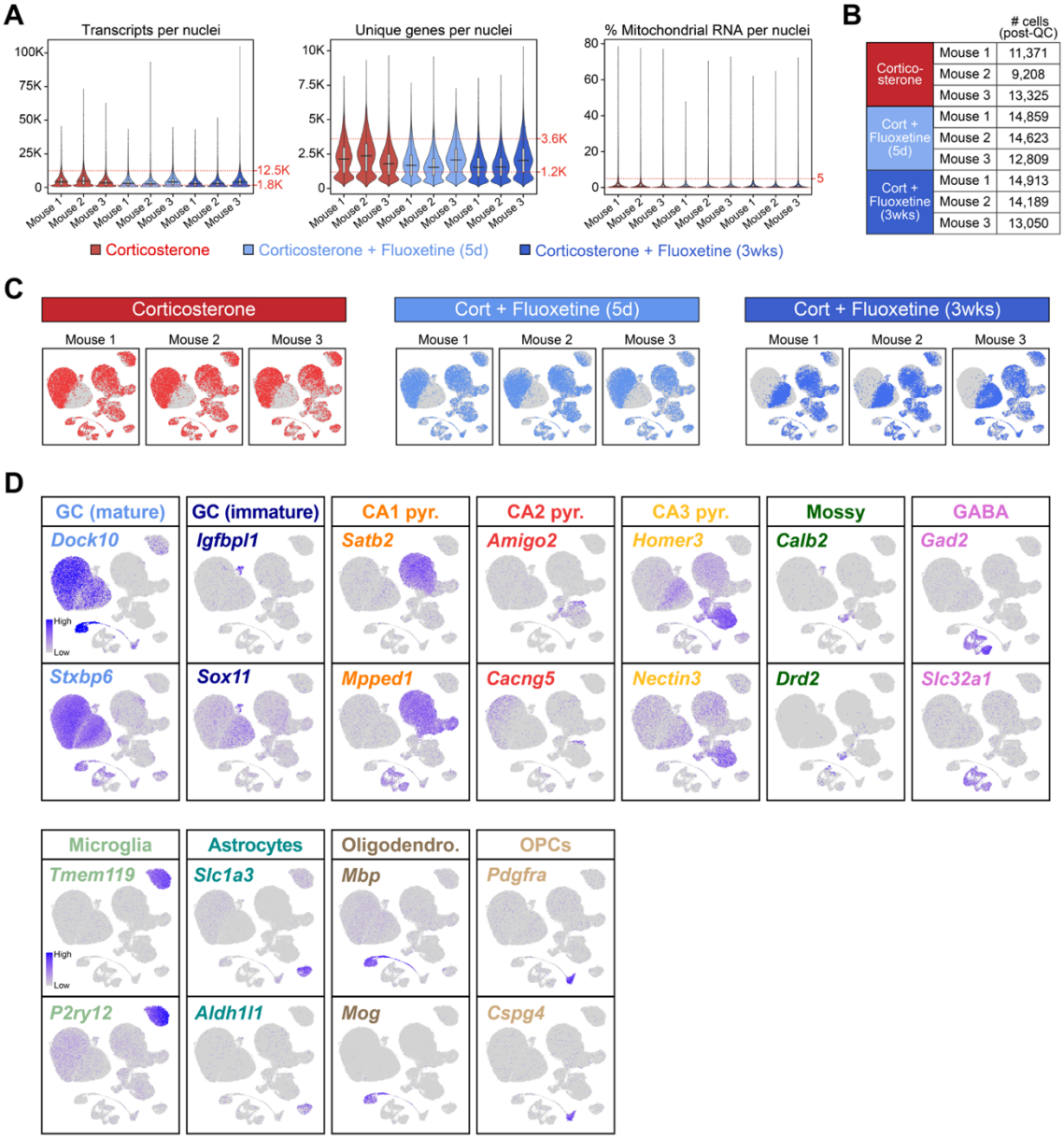

Fig. S2. Quality control and validation of snRNA-seq; related to Figure 2. (**A**) Quality control metrics for single nuclei RNA-sequencing in Cort, Cort + Flx (5d), and Cort + Flx (3wks) groups. Dashed lines indicate minimum and maximum threshold settings. (**B**) Table showing number of nuclei per mouse per condition after quality control thresholding. (**C**) Comparison of biological replicates following unsupervised clustering of hippocampal nuclei. (**D**) Representative markers for each major neuronal and glia cell type in the hippocampus. GC = granule cells (dentate gyrus), Pyr. = pyramidal neuron, Oligodendro. = oligodendrocytes, OPCs = oligodendrocyte progenitor cells.

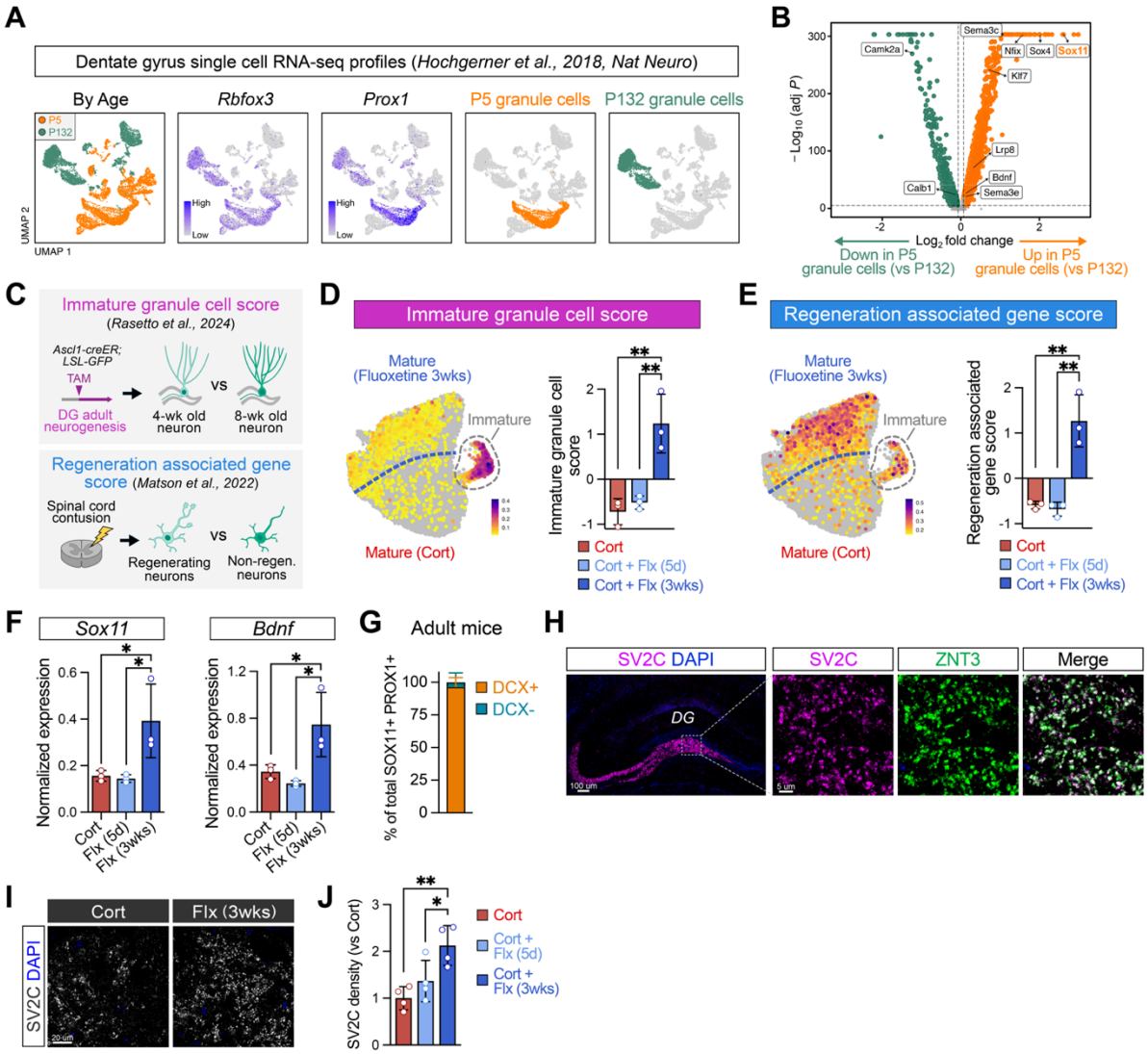

Fig. S3. Additional data pertaining to snRNA-seq and structural plasticity experiments; related to Figure 3. (**A**) Analysis of single cell RNA-seq dataset (*29*) comprised of 8,264 cells from the dentate gyrus from P5 and P132 mice. Unsupervised clustering analysis and identification of granule cells are shown (n = 6 pooled mice (P5), 3 male/1 female mice (P132)). (**B**) Volcano plot of differentially expressed genes in P5 granule cells versus P132 granule cells from (A). (**C**) Immature granule cell and regeneration associated gene scores defined as upregulated genes in 4- versus 8-week old neurons generated from adult hippocampal neurogenesis (*31*) and regenerating versus non-regenerating spinal cord neurons (*32*). (**D**) Feature plot showing average expression of 'immature granule cell score' (left) and z-score per mouse in mature granule cells (right; One-way ANOVA, Tukey's post-hoc test, n=3 mice/group). (**E**) Feature plot showing average expression of 'regeneration associated gene score' (left) and z-score per mouse in mature granule cells (right; One-way ANOVA, Tukey's post-hoc test, n=3 mice/group). (**F**) Normalized expression of *Sox11* and *Bdnf* mRNA in mature granule cells (One-way ANOVA, Tukey's post-hoc test, n=3 mice/group). (**G**) Proportion of DCX+ and DCX- neurons in the SOX11+ PROX1+ granule cell population in adult mice. (**H**) Representative image of SV2C protein levels in the hippocampus. Inset shows higher magnifications of SV2C overlapped with ZNT+ mossy fiber terminals. (**I**) SV2C protein levels in the hilar mossy fiber pathway of adult mice treated with Cort or Cort + Flx (3wks). (**J**) Quantification of SV2C density per mouse (One-way ANOVA, Tukey's multiple comparisons test, n=4 mice/group). Data = mean ± SD. *$p < 0.05$; **$p < 0.01$; ***$p < 0.001$; ****$p < 0.0001$.

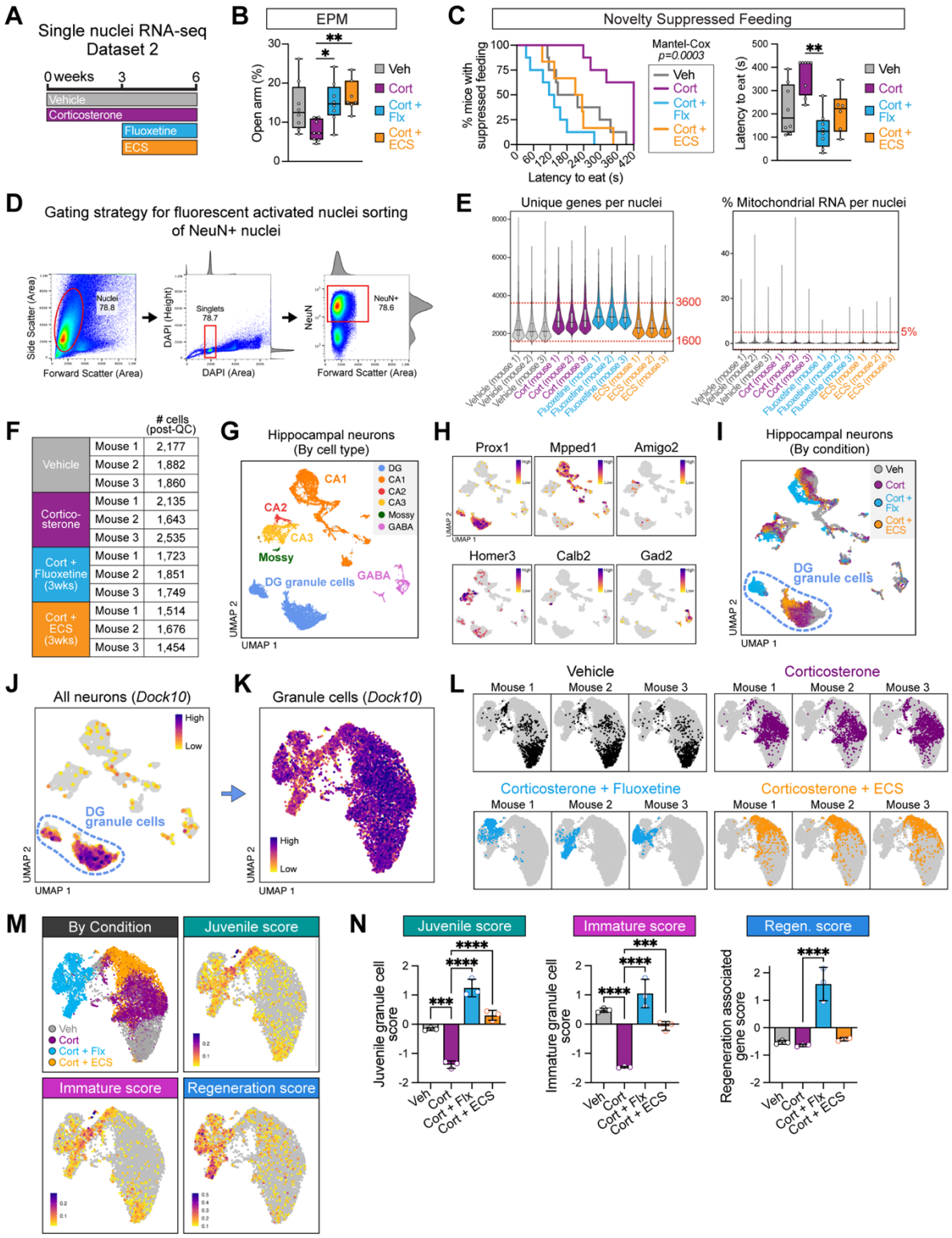

Fig. S4. Reinstatement of developmental plasticity in an independent snRNA-seq dataset with electroconvulsive shock. (**A**) Schematic for pharmacological and electroconvulsive shock (ECS) approach for snRNA-seq of hippocampal nuclei (Dataset 2; see *Methods*). Mice received ECS treatment once every other day for a total of 10 sessions (21 days) starting after 3 weeks of Corticosterone treatment. (**B**) Time spent in the open arm of the EPM per mouse (One-way ANOVA, Tukey's multiple comparisons test, n=8 (Veh), 8 (Cort), 8 (Flx), 7 (ECS)). (**C**) Latency to feed in NSF per mouse shown as survival curve (left; Log-rank Mantel-Cox test, $\chi 2$=18.78, p=0.0003) and box plot (right; Kruskal-Wallis test, Dunn's multiple comparisons test, n= same as (B)). (**D**)

Representative gating strategy to isolate NeuN+ neuronal nuclei from the hippocampus using fluorescence activated nuclei sorting for downstream snRNA-seq. (**E**) Quality control metrics for snRNA-seq in Vehicle, Cort, Cort + Flx, and Cort + ECS groups. Dashed lines indicate minimum and maximum threshold settings. (**F**) Table showing number of nuclei per mouse per condition after quality control thresholding. (**G**) Unsupervised clustering (UMAP) of 22,199 single nuclei transcriptomic profiles of hippocampal neurons labeled by cell type. (**H**) Expression of cell type-specific marker genes for major neuronal populations. (**I**) Hippocampal nuclei labeled by treatment condition: Vehicle (grey), Corticosterone (purple), Cort + Flx (blue), and Cort + ECS (orange). (**J**) Hippocampal nuclei labeled by *Dock10* expression identifies DG granule cells. (**K**) Subclustering of granule cells from (J) and *Dock10* expression. (**L**) Comparison of biological replicates for each treatment condition. (**M**) Granule cell transcriptomic profiles shown by treatment condition and average expression of 'juvenile granule cells score', 'Immature granule cell score', and 'regeneration associated gene score' (see also Fig. 3C and Fig. S3C). (**N**) Quantification of z-scores in mature granule cells per mouse (One-way ANOVA, Tukey's multiple comparisons test, n=3 mice/group). Data = mean ± SD. *$p < 0.05$; **$p < 0.01$; ***$p < 0.001$; ****$p < 0.0001$.

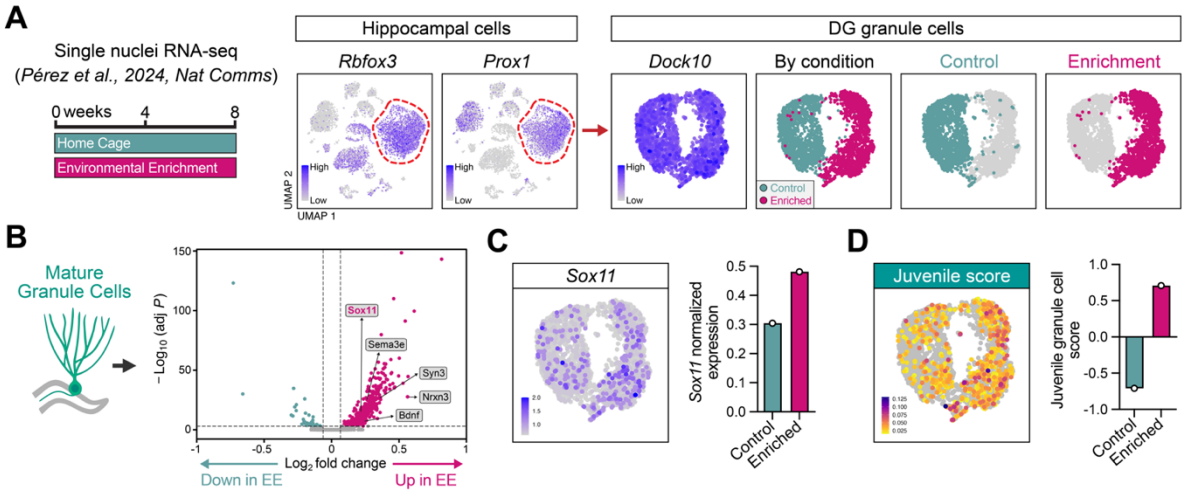

Fig. S5. Reinstatement of developmental plasticity in mature granule cells after environmental enrichment. (**A**) Analysis of single nuclei RNA-seq dataset (*41*) comprised of 7,217 hippocampal cells from 9 week-old mice exposed to environmental enrichment (2 months) or control cages. Unsupervised clustering analysis, identification, and subclustering of DG granule cells (3,097 nuclei) are shown (n = 3 mice pooled into 1 replicate per condition). (**B**) Volcano plot of differentially expressed genes in mature granule cells from enriched versus control mice reveals *Sox11* upregulation after enrichment. (**C**) Feature plot showing *Sox11* expression in mature granule cells (left) and quantification of normalized expression per mouse (right). (**D**) Feature plot showing average expression of 'juvenile granule cell score' (left; see also Fig. 3C) and z-scores in mature granule cells per mouse (right).